THE ASTROPHYSICAL JOURNAL, 417:624–644, 1993 November 10

EXTREMELY HIGH VELOCITY OUTFLOWS

MINHO CHOI,[1] NEAL J. EVANS II,[2] AND DANIEL T. JAFFE[3]
Department of Astronomy, University of Texas at Austin, Austin, Texas 87812-1083
Received 1992 December 21; accepted 1993 May 13

ABSTRACT

Extremely high velocity (EHV) wings, with full widths of 72 to 140 km s^{-1}, are seen on the CO $J = 3 \rightarrow 2$ lines toward W3 IRS 5, GL 490, NGC 2071, W28 A2 (G05.89−0.39), GL 2591, S140, and Cepheus A. Observations of ^{12}CO and ^{13}CO $J = 3 \rightarrow 2$ and $J = 2 \rightarrow 1$ lines indicate that optical depth generally decreases with increasing velocity separation from the ambient cloud velocity. Maps of the extremely high velocity ($|V - V_0| \gtrsim 20$ km s^{-1}) and the high-velocity ($5 \lesssim |V - V_0| \lesssim 20$ km s^{-1}) CO emission components show that the morphology of the two components is similar in W3 IRS 5 and W28 A2 but may be different in GL 2591, S140, and Cepheus A.

The results of our survey suggest that EHV wings are common around infrared sources of moderate to high luminosity [500 to (4×10^5) $L_\odot$] in dense regions. Line ratios imply that the EHV gas is usually optically thin and warm. Characteristic velocities range from 20 to 40 km s^{-1}, yielding timescales of 1600–4200 yr. Since most sources in this study are producing some ionizing photons, these short timescales suggest that neutral winds coexist with ionizing photons.

We examined two possible sources for the extremely high velocity CO emission: a neutral stellar wind; and swept-up or entrained molecular gas. Neither can be ruled out. If the high-velocity (HV) gas is swept up by a momentum-conserving stellar wind traced by the extremely high velocity CO emission, most of the C in the winds from luminous objects cannot be in CO. If the EHV and HV forces are equal, the fraction of C in a form other than CO increases with source luminosity and with the production rate of ionizing photons. This trend is natural in the stellar wind hypothesis, but models of winds around such luminous objects are needed. We consider other possible chemical states for the carbon in the stellar wind.

Subject headings: ISM: jets and outflows — ISM: kinematics and dynamics — ISM: molecules

1. INTRODUCTION

Molecular outflows are common in regions of star formation (about 200 known: Lada 1985; Fukui et al. 1993; Bachiller & Gómez-González 1992). High-velocity (hereafter HV) molecular flows—with velocities ranging from a few km s^{-1} to about 20 km s^{-1}—have been studied extensively (Bally & Lada 1983; Plambeck, Snell, & Loren 1983; Snell et al. 1984; Richardson et al. 1985; Phillips et al. 1988). These molecular outflows most likely consist of ambient cloud material swept up by a faster stellar wind (Snell, Loren, & Plambeck 1980).

Searches for an ionized fast stellar wind to drive the HV gas found that the momentum in the ionized gas was inadequate to sweep up the observed amount of molecular material (Rodríguez & Cantó 1983; Evans et al. 1987), leading to the suggestion that the stellar wind was primarily neutral (Natta et al. 1988). The neutral wind gained support from the discovery of very wide wings on the spectra of H I emission (Lizano et al. 1988; Giovanardi et al. 1992) toward several young stars. Lizano et al. (1988), Koo (1989, 1990), and Margulis & Snell (1989) also recognized extremely high velocity (hereafter EHV) wings on the CO spectra toward a few sources, suggesting that there might be CO in the stellar wind itself. In recent years, there have been additional observations of EHV CO outflows (Bachiller & Cernicharo 1990; Masson, Mundy, & Keene 1990; Bachiller, Martín-Pintado, & Planesas 1991; Mitchell & Hasegawa 1991; Chernin & Masson 1992; Richer, Hills, & Padman 1992). Stahler (1993) has suggested that EHV outflows are the manifestation in young objects of the optical jets seen in later phases of evolution.

Calculations of the chemistry in stellar winds from low-mass stars indicated that CO could form in the neutral wind (Glassgold, Mamon, & Huggins 1989). Later calculations of the thermal structure of these winds (Ruden, Glassgold, & Shu 1990) agreed with that conclusion, and new chemical models which incorporated the thermal structure found that, for mass-loss rates $\dot{M} \geq 3 \times 10^{-6}$ $M_\odot$ yr^{-1} virtually all of the carbon is in CO ([CO]/[H] = 4×10^{-4}), even though the hydrogen remains mostly atomic, unless $\dot{M} \geq 10^{-4}$ $M_\odot$ yr^{-1} (Glassgold, Mamon, & Huggins 1991).

The thermal models of Ruden et al. (1990) raised questions, however, about whether a wind could maintain the high temperature ($T_K \approx 100$ K) and density ($n > 10^4$ cm^{-3}) deduced by Koo (1989) for HH 7–11, on large enough scales ($\sim$0.1 pc) to be consistent with the observations. In addition, Masson et al. (1990) and Bachiller & Cernicharo (1990) found relatively narrow ($\Delta V \approx 20$ km s^{-1}) spectral features at extremely high velocities ($|V - V_0| \approx 150$ km s^{-1}), displaced from the center of the outflow in HH 7–11, suggesting that the EHV gas consists of discrete blobs, rather than a continuous wind. Similar discrete EHV spectral features exist in several other sources (Bachiller et al. 1990, 1991; Bachiller & Gómez-González 1992). The blobs may be related to Herbig-Haro objects and to localized EHV spectral features often found in H_2O maser observations of compact H II regions (Genzel & Downes 1977, 1979).

The nature of the EHV CO emission is currently unclear. It

[1] Electronic mail: minho@astro.as.utexas.edu
[2] Electronic mail: nje@astro.as.utexas.edu
[3] Electronic mail: dtj@astro.as.utexas.edu

TABLE 1

OBSERVATIONAL PARAMETERS

Telescope	Transition	ν (GHz)	Δv[a] (km s^{-1})	θ[b]	η_{mb}[c]
CSO.....	^{13}CO $J = 2 \rightarrow 1$	220.3987	1.37	32″	0.71
	CO $J = 2 \rightarrow 1$	230.5380	1.28	30	0.71
	^{13}CO $J = 3 \rightarrow 2$	330.5880	0.91	21	0.55
	CO $J = 3 \rightarrow 2$	345.7960	0.86	20	0.55

[a] Velocity resolution in km s^{-1}.
[b] Beam size (FWHM) in arcseconds.
[c] Main beam efficiency (Mangum 1993).

could arise in the stellar wind, or it could be ambient molecular gas which has been entrained or swept up (see Bachiller & Gómez-González 1992 and Stahler 1993 for excellent reviews).

While observing the CS $J = 7 \rightarrow 6$ line toward several sources, we notices EHV wings on the CO $J = 3 \rightarrow 2$ lines, which appear in the opposite sideband. We followed up by mapping the EHV gas in CO $J = 3 \rightarrow 2$ emission and by obtaining data on other transitions. In this paper, we report observations of W3 IRS 5, GL 490, NGC 2071, W28 A2, GL 2591, S140, and Cepheus A. Most previous detections of EHV wings have been toward sources of low to moderate luminosity ($L < 1000\ L_\odot$); this work extends the phenomenon to higher luminosity sources. These sources, some of which are generating ionizing photons, may have different wind properties if ionization plays a role in the wind generation process or in the chemical composition of the wind.

We describe our observations in § 2. Section 3 explains the analysis we used to get physical parameters from the observations (optical depth, excitation temperature, mass, etc.). We summarize our analysis and discuss its implications in § 4.

2. OBSERVATIONS AND DATA REDUCTION

We made all observations with the 10.4 m telescope of the Caltech Submillimeter Observatory (CSO)[4] at Mauna Kea during several runs between 1989 June and 1992 February. At the central position, all sources were observed in four molecular transitions: CO $J = 3 \rightarrow 2$, CO $J = 2 \rightarrow 1$, ^{13}CO $J = 3 \rightarrow 2$, and ^{13}CO $J = 2 \rightarrow 1$. Since most of the sources show much brighter CO $J = 3 \rightarrow 2$ wings than CO $J = 2 \rightarrow 1$ wings, they were mapped in the CO $J = 3 \rightarrow 2$ line. Table 1 summarizes the observational parameters. The data were obtained using the 230 GHz and 345 GHz SIS receivers in double-sideband mode with a 500 MHz AOS spectrometer as the backend. Telescope pointing was checked by observing CRL 618, CRL 2688, or Jupiter regularly and was consistent to within $\sim 5''$.

The data were taken by position switching. Table 2 lists the central and the OFF positions. For each source, an effort was made to acquire at least some of the data with an OFF position which was free of CO emission in the line core. Since some of these OFF positions were quite distant, other data were taken with more nearby OFF positions to improve the baselines. Therefore, the line cores in the figures may be affected by emission in the OFF positions. Some sources were observed repeatedly over several runs and the intensities were consistent to within $\sim 10\%$.

The antenna temperature (T_A^*) was calibrated by the standard chopper-wheel method, which automatically corrected, to first order, for the effects of atmospheric attenuation. The radiation temperature, T_R, following the notation of Kutner & Ulich (1981), was obtained by dividing T_A^* by the telescope main beam efficiency ($\eta_{mb} = \eta_b/\eta_{rss}$, where η_b is the beam efficiency defined by Kraus (1966) and η_{rss} is the rear spillover and scattering efficiency; see Table 1). We determined η_b by observations of planets, primarily Jupiter (Mangum 1993). Thus, the calibration is appropriate for sources which fill the main beam. For sources smaller than the main beam, filling factors must be considered. Since the beam was about 30″ for the $J = 2 \rightarrow 1$ data and 20″ for the $J = 3 \rightarrow 2$ data, a point source centered in both beams will have a filling factor for the $J = 3 \rightarrow 2$ data which is $(3/2)^2$ times as high as that for the $J = 2 \rightarrow 1$ data. For the CO $J = 3 \rightarrow 2$ observations, the CS $J = 7 \rightarrow 6$ appears in the image sideband. The velocity of the telescope with respect to the LSR was different on each run; as a result, the intensities and shapes of the CS $J = 7 \rightarrow 6$ lines in Figures 1*a*–7*a* are not correct, and in some spectra, the CS line appears twice.

The data were averaged for each line and a baseline was removed, using the velocity ranges listed under Baseline in Table 3. For the CO $J = 3 \rightarrow 2$ line, the region of the CS $J = 7 \rightarrow 6$ line was also excluded from the baseline fit. At the central positions, where we take line ratios, first-order base-

[4] The CSO is operated by the California Institute of Technology under funding from the National Science Foundation, contract AST 90-15755.

TABLE 2

SOURCE PARAMETERS

Source	α_{1950}	δ_{1950}	d[a] (kpc)	References	$\Delta\alpha$[b]	$\Delta\delta$[b]	Line[c]
W3 IRS 5	02^{h}21^{m}53^s.1	61°52′22″	2.3	1	2400″	0″	3–2, ^{13}3–2, ^{13}2–1
					1200	0	2–1
GL 490	03 23 39.2	58 36 36	1.0	2	−1800	0	3–2, 2–1, ^{13}3–2, ^{13}2–1
NGC 2071	05 44 30.6	00 20 42	0.39	3	−2700	900	3–2, ^{13}3–2, ^{13}2–1
					−2700	0	2–1
W28 A2.....	17 57 26.8	−24 03 54	3.0	4	−600	0	3–2, 2–1, ^{13}3–2, ^{13}2–1
GL 2591	20 27 35.8	40 01 14	2.0	5	0	10800	3–2, 2–1, ^{13}3–2, ^{13}2–1
S140	22 17 41.2	63 03 45	0.91	6	−600	−600	3–2, 2–1, ^{13}3–2, ^{13}2–1
Cepheus A.....	22 54 19.0	61 45 47	0.725	7	−780	0	3–2, 2–1, ^{13}3–2
					0	1200	^{13}2–1

[a] Distance from the Sun in kpc.
[b] Coordinates of OFF positions relative to the central position.
[c] 3–2: CO $J = 3 \rightarrow 2$; ^{13}3–2: ^{13}CO $J = 3 \rightarrow 2$; 2–1: CO $J = 2 \rightarrow 1$; ^{13}CO $J = 2 \rightarrow 1$.

REFERENCES.—(1) Georgelin & Georgelin 1976; (2) Snell et al. 1984; (3) Anthony-Twarog 1982; (4) Harvey & Forveille 1988; (5) Merrill & Soifer 1974; (6) Crampton & Fisher 1974; (7) Blaauw, Hiltner, & Johnson 1959.

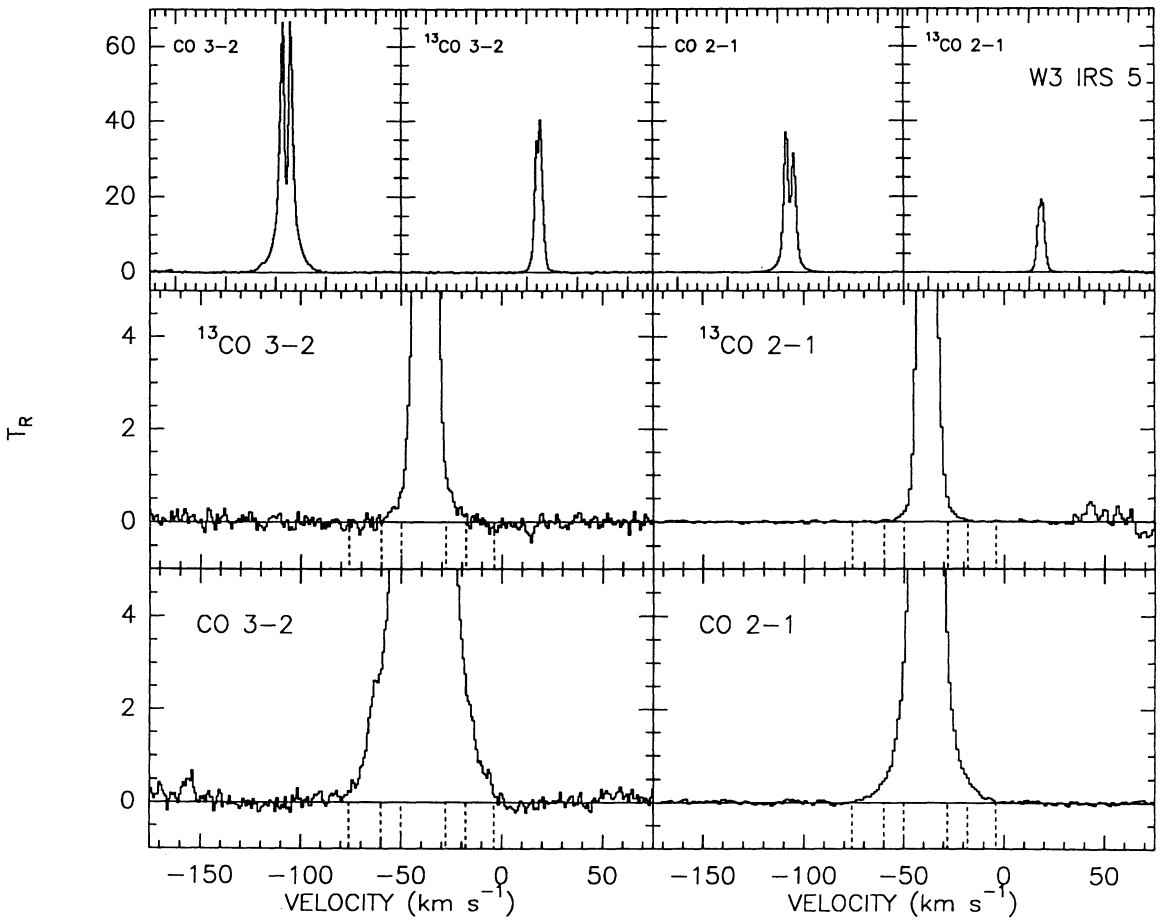

FIG. 1*a*

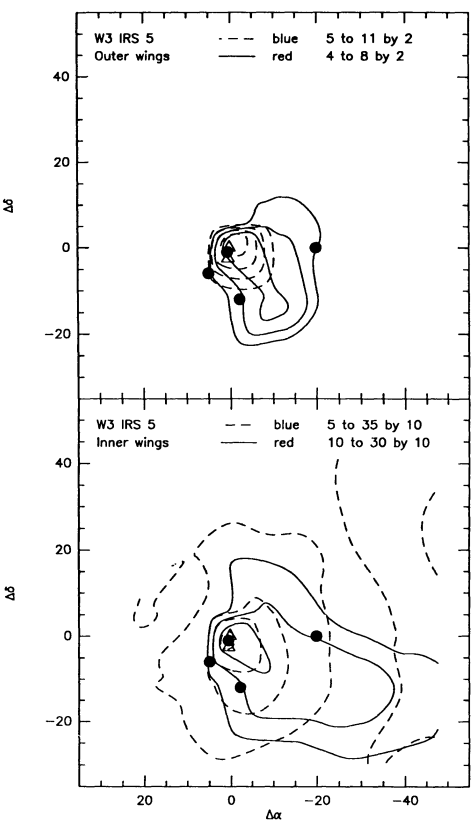

FIG. 1*b*

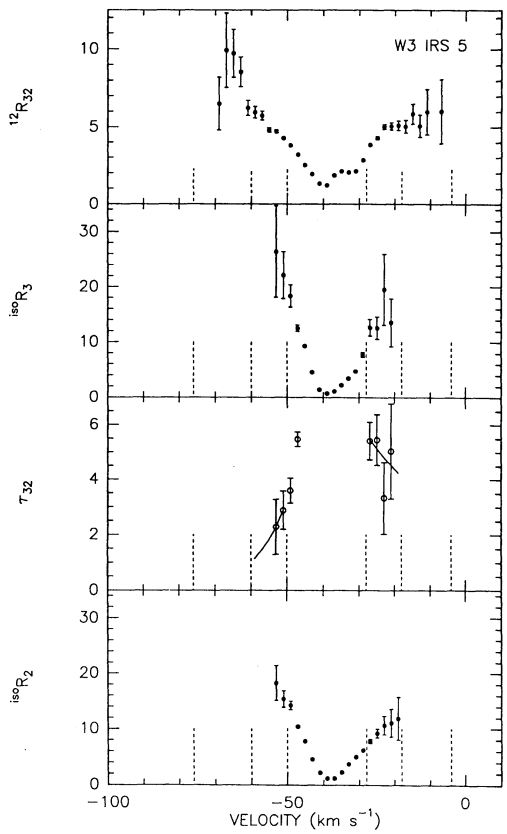

FIG. 1*c*

TABLE 3

LINE PARAMETERS

Source	Line[a]	Baseline[b]	Noise[c] (K)	Threshold[d] (K)
W3 IRS 5	3–2	(−150, −90), (10, 40)	0.115	0.264
	2–1	(−150, −90), (30, 100)	0.038	0.096
	^{13}3–2	(−150, −70), (0, 100)	0.116	0.285
	^{13}2–1	(−150, −70), (0, 30)	0.019	0.048
GL 490	3–2	(−100, −75), (50, 100)	0.056	0.126
	2–1	(−100, −80), (50, 100)	0.155	0.297
	^{13}3–2	(−100, −50), (40, 100)	0.291	0.645
	^{13}2–1	(−100, −50), (40, 100)	0.114	0.264
NGC 2017	3–2	(−130, −60), (100, 150)	0.091	0.195
	2–1	(−130, −60), (90, 150)	0.035	0.084
	^{13}3–2	(−130, −60), (90, 150)	0.064	0.135
	^{13}2–1	(−130, −50), (60, 150)	0.035	0.084
W28 A2	3–2	(−100, −90), (180, 220)	0.225	0.579
	2–1	(−200, −100), (100, 150)	0.090	0.228
	^{13}3–2	(−180, −80), (70, 180)	0.222	0.546
	^{13}2–1	(−150, −100), (100, 150)	0.211	0.516
GL 2591	3–2	(−120, −50), (25, 85)	0.211	0.528
	2–1	(−120, −50), (25, 85)	0.070	0.180
	^{13}3–2	(−120, −50), (25, 85)	0.189	0.432
	^{13}2–1	(−120, −40), (20, 85)	0.026	0.072
S140	3–2	(−90, −60), (30, 80)	0.084	0.219
	2–1	(−100, −60), (30, 100)	0.046	0.117
	^{13}3–2	(−100, −60), (30, 100)	0.078	0.180
	^{13}2–1	(−100, −60), (30, (100)	0.037	0.102
Cepheus A	3–2	(−200, −150), (80, 120)	0.422	0.900
	2–1	(−150, −100), (100, 150)	0.285	0.639
	^{13}3–2	(−100, −50), (30, 100)	0.120	0.306
	^{13}2–1	(−100, −50), (30, 100)	0.027	0.069

[a] See Table 2.
[b] Intervals considered in the baseline determination in km s^{-1}
[c] RMS of noise with the resolution in Table 1.
[d] Thresholds for the line ratios in data with $\Delta v = 2$ km s^{-1}.

lines were used. The resulting RMS noise levels in the baselines are given in Table 3 and spectra are shown in Figures 1*a*–7*a*. Both a full-scale plot and a blowup are shown to indicate the range and quality of the baselines. From the blown-up spectra, one can see that the full widths to where the wing vanishes into the noise range from 72 km s^{-1} for W3 IRS 5 to 140 km s^{-1} for W28 A2 (Table 4).

The mapping data were taken with shorter integration times, so their quality is lower. First-order baselines were also used for most of these spectra, but a few off-center positions required baselines up to third order.

Since we are interested in the differences between HV components and EHV components of outflows, we have defined the inner and outer wings by examination of the CO $J = 3 \rightarrow 2$ spectra. For about half of our sources, the boundary between the inner and outer wings was set by noticing a distinct change in the CO $J = 3 \rightarrow 2$ line profile, marked by the appearance of a component which declines more slowly with velocity away from the line core. For sources without a distinct change of slope, we set the boundary between our inner and outer wings at the largest velocity at which wings were previously known. For W28 A2, the boundaries between inner and outer wings are quite subjective because it is difficult to find a distinct change of slope and there is no reference useful to define the boundary. The average velocity offset from the line center for the boundary between inner and outer wings was 21 km s^{-1}, corresponding roughly to the boundaries chosen in other studies (e.g., Koo 1990) making it a reasonable, if not precise, choice for separating HV and EHV emission. The outer boundaries of the outer wings were set by our subjective assessment of the extremes of detectable wings. The wing boundaries are listed in Table 4 and marked in the blown-up spectra and the line ratio plots by dashed vertical lines.

After defining the wing boundaries, we integrated the intensity between the boundaries and plotted the results as contour maps. We always set the lowest contour level higher than twice the RMS noise.

To assess the optical depths in the wings, we examined various ratios of lines as a function of velocity. We resampled the spectra toward the central positions to a resolution of 2 km s^{-1} and formed the following line ratios: $^{12}R_{32}$, CO $J = 3 \rightarrow 2$ line divided by CO $J = 2 \rightarrow 1$; $^{iso}R_3$, CO $J = 3 \rightarrow 2$ divided by ^{13}CO $J = 3 \rightarrow 2$; and $^{iso}R_2$, CO $J = 2 \rightarrow 1$ divided by ^{13}CO $J = 2 \rightarrow 1$. The results (Figs. 1*c*–7*c*) were blanked from the plot beyond the velocity where either the numerator or the denominator fell below the threshold (3 times the RMS noise in the resampled spectra) in Table 3.

3. ANALYSIS

In this section, we describe how we determined optical depths, excitation temperatures, and column densities from the line ratios. We also explain our calculations of the mass, momentum, and kinetic energy in the outflowing gas. We then compare the driving force in the EHV gas to that in the HV gas, compute timescales for the outflows, and collect data on the stellar luminosity and the production rate of ionizing photons.

FIG. 1.—(*a*) CO spectra of W3 IRS 5 with baselines. The upper four panels show the full spectra of the lines, and the middle and lower four panels have blown-up vertical scales to show the details of the wings. All the horizontal axes cover the same velocity extent. Vertical dashed lines below the baselines are the wing boundaries (also given in Table 4). (*b*) Contour maps of the integrated intensity for each wing of W3 IRS 5 in the CO $J = 3 \rightarrow 2$ line. The lower panel shows the maps of the inner wings, and the upper panel shows those of the outer wings. Solid contours are for red wings, and dashed contours for blue wings. At the upper right corner of each panel are the integrated antenna temperature ($\int T_A^* dV$) of the lowest contour level, the highest contour level, and the spacing between contours in K km s^{-1}. Maps were made with a 12″ grid. Maps also include markers at the positions of IRS 6, IRS 5, IRS 7, and IRS 3 (*filled circles*) from left to right (Wynn-Williams, Becklin, & Neugebauer 1972), and H_2O maser sources (*open triangles*) from Forster, Welch, & Wright (1977). The maps of the outer wings show a compact source centered at or near IRS 5. The emission in the red wing appears slightly extended toward the southwest (cf. Mitchell et al. 1991; Claussen et al. 1984). (*c*) At the central position of W3 IRS 5, the line ratio (T_R) of CO $J = 3 \rightarrow 2$ to $J = 2 \rightarrow 1$ in the top panel, CO $J = 3 \rightarrow 2$ to ^{13}CO $J = 3 \rightarrow 2$ in the second panel, optical depth of CO $J = 3 \rightarrow 2$ line in the third panel, and line ratio of CO $J = 2 \rightarrow 1$ to ^{13}CO $J = 2 \rightarrow 1$ in the bottom panel. Values for line ratios have been left out whenever T_R's drop below the thresholds given in Table 3. Vertical dashed lines are the wing boundaries. Solid exponential curves in the inner wings in the third panel are the least-squares fits of τ_{32}. For the outer wings, we assumed $\tau_{32} \ll 1$. The line ratios $^{12}R_{32}$, $^{iso}R_3$, and $^{iso}R_2$ rise toward the line wings until they become undefined because the line in the divisor is too weak. The ratio $^{12}R_{32}$ implies low optical depth, even for the inner wings. Even assuming the maximum ratio for the beam filling factors, $^{12}R_{32}$ becomes large enough to require $\tau_{32} < 1$ for inner and outer wings, contrary to the τ_{32} calculated from $^{iso}R_3$. In fact, $^{12}R_{32}$ is illegally high [$> (3/2)^4$] at some channels in the outer wings, perhaps because of a pointing error in the CO $J = 2 \rightarrow 1$ data (note that the blue EHV outflow of W3 IRS 5 is the most compact among the sources in this paper). Nonetheless, we interpret the high ratios as strong evidence for optically thin emission.

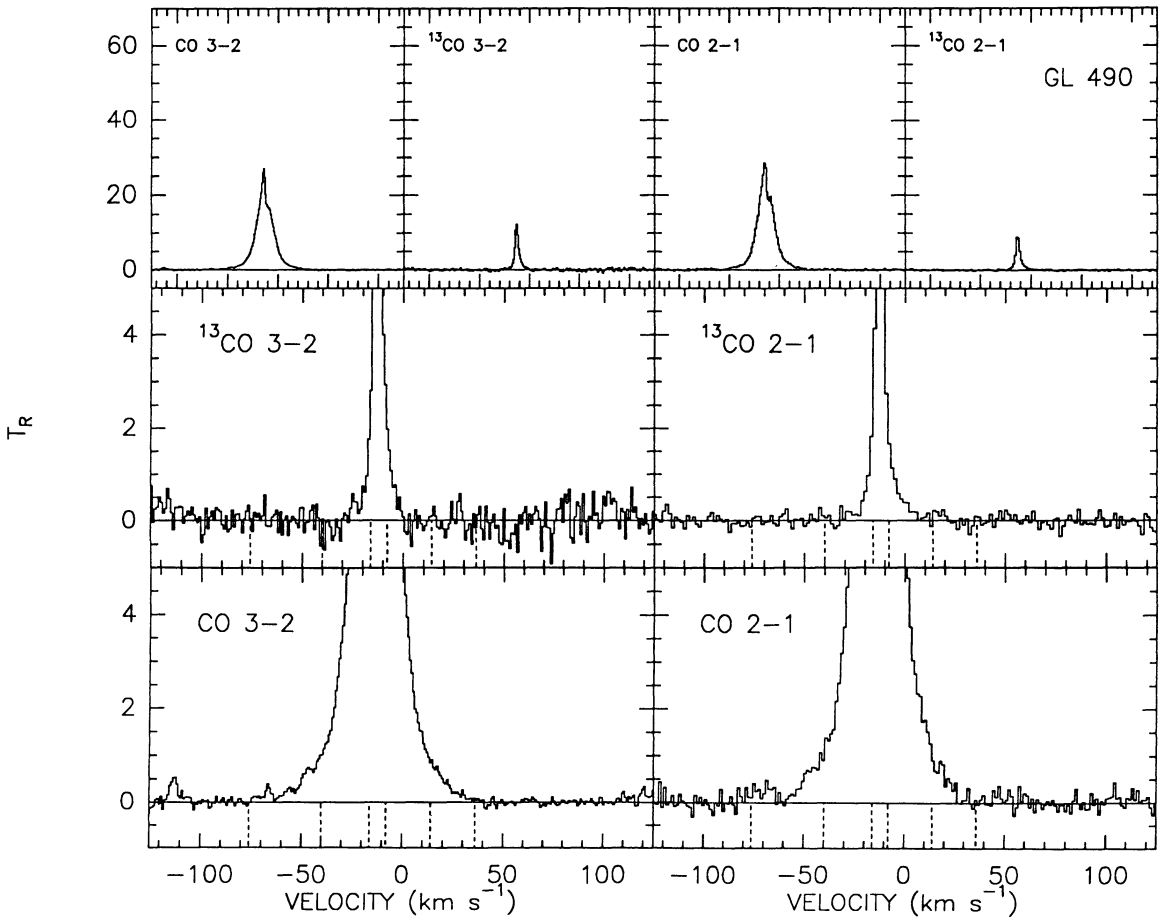

FIG. 2*a*

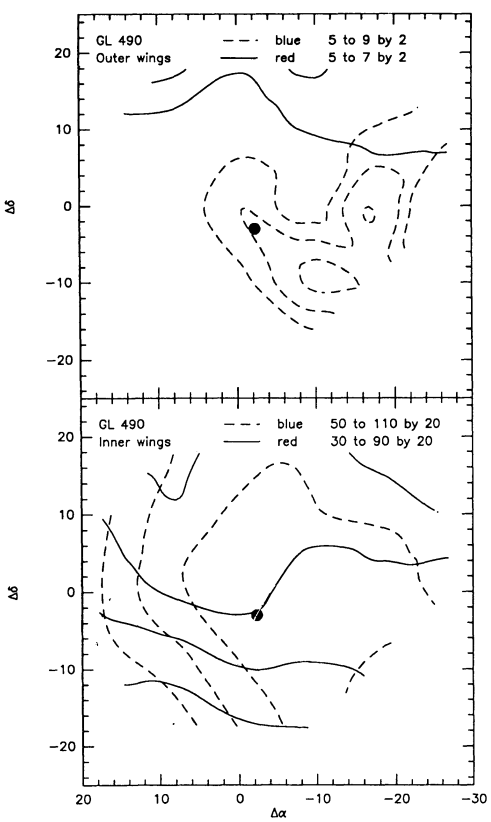

FIG. 2*b*

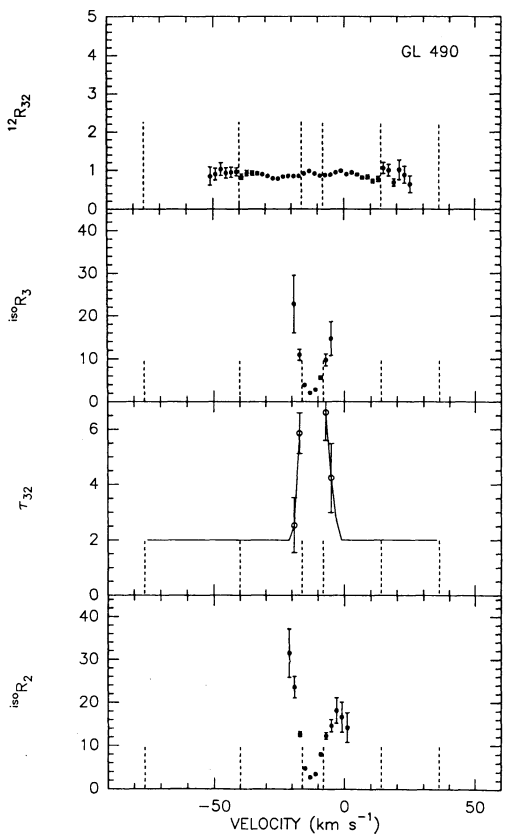

FIG. 2*c*

TABLE 4

WING BOUNDARIES

SOURCE	BLUE Outer	BLUE Inner	V_0	RED Inner	RED Outer		FULL WIDTH OF WING	NOTES
W3 IRS 5	−76	−60[a]	−50	−37	−28	−18[a]	−4	72	
GL 490	−76	−40[b]	−16	−13	−8	14[b]	36	112	1
NGC 2071	−50	−10[a]	0	11	18	28[a]	68	118	2
W28 A2.....	−70	−20[c]	2	9	18	32[c]	70	140	3
GL 2591	−49	−21[a]	−11	−6	3	15[a]	25	74	4
S140	−56	−30[b]	−12	−7	−4	6[a]	30	86	5
Cepheus A.....	−81	−29[a]	−17	−12	−5	7[a]	51	132	6

NOTE.—All velocities are in km s^{-1}.

[a] The boundaries between inner and outer wings were set by noticing distinct changes of the slope in the CO $J = 3 \rightarrow 2$ spectra.

[b] The CO $J = 3 \rightarrow 2$ spectra do not show clear change of slope, and the inner wings were defined from previous observations of HV outflows.

[c] The CO $J = 3 \rightarrow 2$ spectra do not show clear change of slope, and the boundaries between inner and outer wings were set subjectively.

NOTES.—(1) GL 490.—Our inner wings coincide with the wings seen by Snell et al. 1984. The full widths of the EHV CO $J = 1 \rightarrow 0$ line of Koo 1989 and Margulis & Snell 1989 are wider than ours by 40 and 13 km s^{-1}, respectively, probably because of higher signal-to-noise ratios. (2) NGC 2071.—Our inner wings coincide with the entire wings seen by Bally 1982, while our outer wings are wider by ~40 km s^{-1} on each side, similar to those of Chernin & Masson 1992. (3) W28 A2.—The full width of the wings is comparable to the width in CO $J = 1 \rightarrow 0$ line (Harvey & Forveille 1988). (4) GL 2591.—Our inner wings have the same boundaries as defined in Lada et al. 1984 and are similar to those of Mitchell, Maillard, & Hasegawa 1991. (5) S140.—Our inner blue wing has the same extent as the blue wing of Hayashi et al. 1987 and Snell et al. 1984. The full width of the EHV CO $J = 1 \rightarrow 0$ line of Koo 1989 is wider than ours by 30 km s^{-1}, but that of Margulis & Snell 1989 is narrower than ours by 11 km s^{-1}. (6) Cepheus A.—Our inner wings correspond to the wings shown in Figs. 3*b*–3*g* of Ho, Moran, & Rodríguez 1982. Our outer blue wing is wider than the wing in Fig. 3*h* of Ho et al. 1982, and our outer red wing was seen by them.

3.1. *Optical Depth*

From the isotopic line ratio, ${}^{iso}R_3$, we calculated τ_{32}, the optical depth of the CO $J = 3 \rightarrow 2$ line in each channel, from

$$ {}^{iso}R_3 = \frac{T_{R3-2}}{T_{R(13)3-2}} = \frac{1 - \exp(-\tau_{32})}{1 - \exp(-\tau_{32}/X)}, \quad (1) $$

where X (listed in Table 5) is the isotopic abundance ratio, [CO]/[^{13}CO]. We assumed that X is a linear function of distance from the Galactic center (Langer & Penzias 1990) except for NGC 2071, where we assumed $X = 73$, the average for Ori A. The low strength in the outer wings of ^{13}CO lines means that most sources do not have well-defined ${}^{iso}R_3$ at extremely high velocities.

One way to constrain the optical depth at extremely high velocities is through the ratio of the CO $J = 3 \rightarrow 2$ lines and $J = 2 \rightarrow 1$ lines; the ratio is given by

$$ {}^{12}R_{32} = \frac{T_{R3-2}}{T_{R2-1}} = \phi \frac{[J_{\nu 32}(T_{ex}) - J_{\nu 32}(T_{bk})]}{[J_{\nu 21}(T_{ex}) - J_{\nu 21}(T_{bk})]} \frac{[1 - \exp(-\tau_{32})]}{[1 - \exp(-\tau_{21})]}, \quad (2) $$

where ϕ is the ratio of beam filling factors which accounts for differences in telescope beam sizes, $J_\nu(T)$ is the Planck function in temperature units, T_{ex} is the excitation temperature (assuming that the two lines have the same excitation temperature), and $T_{bk} = 2.7$ K. In the limits of $\tau \rightarrow 0$ and $T_{ex} \rightarrow \infty$, ${}^{12}R_{32}$ approaches $(\nu_{32}/\nu_{21})^2 = (3/2)^2$ (for an extended source) or $(\nu_{32}/\nu_{21})^4 = (3/2)^4$ (for a point source centered in both beams) as shown in Figure 10 (Appendix A).

Most of the sources have ${}^{iso}R_3$ ratios which increase away from the line center and ${}^{12}R_{32}$ ratios which imply low optical depth in the outer wings. We assumed that the outer wings were optically thin, except for the red wing of S140 and both wings of GL 490, for which ${}^{12}R_{32}$ is relatively low. For these wings we assumed $\tau_{32} = 2$ (which is chosen arbitrarily) for all velocities. For the inner wings, we fitted τ_{32}, determined from ${}^{iso}R_3$, with an exponential function ($\tau_{32} = \alpha \exp[\beta(V - V_0)]$, where α and β are constants determined by a least-squares fit) for each side of the spectrum (Figs. 1*c*–7*c*).

3.2. *Excitation Temperature*

For most of the outer wings, the optical depth is low and we can calculate T_{ex} with ${}^{12}R_{32}$ averaged over the wing intervals from

$$ {}^{12}R_{32} = \phi \frac{[J_{\nu 32}(T_{ex}) - J_{\nu 32}(T_{bk})]}{[J_{\nu 21}(T_{ex} - J_{\nu 21}(T_{bk})]} \frac{\tau_{32}}{\tau_{21}}; \quad (3) $$

assuming LTE,

$$ \frac{\tau_{32}}{\tau_{21}} = \frac{3}{2} \frac{1 - \exp(-16.597/T_{ex})}{\exp(11.065/T_{ex}) - 1}. \quad (4) $$

FIG. 2.—(*a*) The same as Fig. 1*a* for GL 490. Only 490 has CO $J = 2 \rightarrow 1$ wings as strong as the CO $J = 3 \rightarrow 2$ wings. The $J = 1 \rightarrow 0$ line is also comparable in strength to the $J = 2 \rightarrow 1$ line over the velocity interval of the inner wings (Margulis & Lada 1985). (*b*) The same as Fig. 1*b* for GL 490. Maps were made with a 9″ grid. For the maps of red wings the lowest contours are the southernmost ones. Markers indicate the position of an infrared source (*filled circles*) from McGregor, Persson, & Cohen (1984). The radio continuum source is coincident with the infrared source. Our map does not cover the whole outflow region and does not reveal a clear morphology. (*c*) The same as Fig. 1*c* for GL 490. The ratio ${}^{12}R_{32}$ is ~0.9 throughout the line core and the wings, suggesting that the gas is cold ($T_{ex} \lesssim 50$ K) and/or the wings are optically thick, even at extremely high velocities. So we assumed that τ_{32} is 2 in the EHV wings.

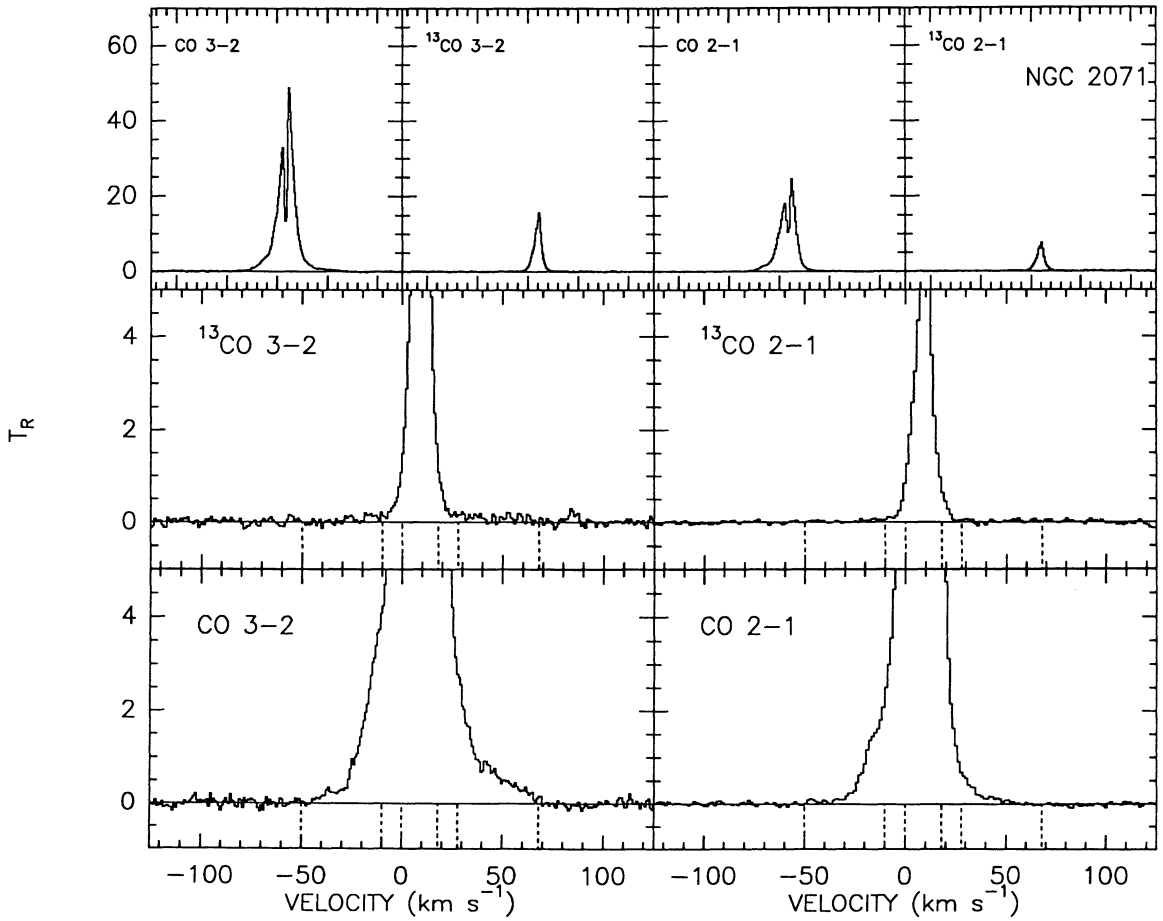

FIG. 3*a*

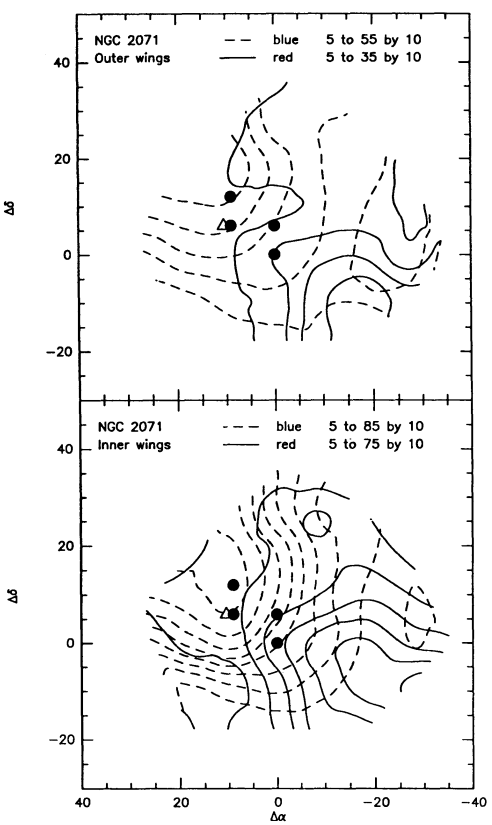

FIG. 3*b*

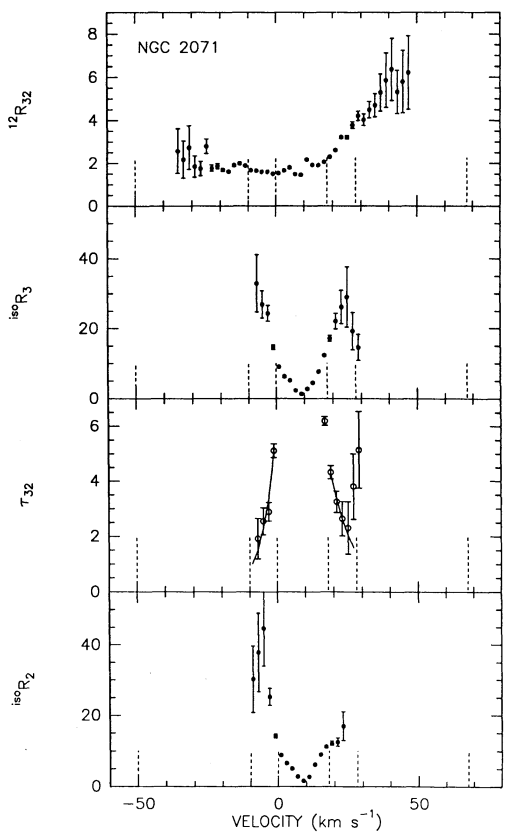

FIG. 3*c*

TABLE 5

PHYSICAL PARAMETERS OF OUTFLOWS

Source	Wing	X^a	$T_{ex}{}^b$ (K)	M^c ($M_\odot$)	M^d ($M_\odot$)	P^c ($M_\odot$ km s^{-1})	P^d ($M_\odot$ km s^{-1})	$E_K{}^c$ (10^{45} ergs)	$E_K{}^d$ (10^{45} ergs)
W3 IRS 5	Outer blue	66	...	0.014	0.11	0.38	3.1	0.11	0.87
	Inner blue		...	...	1.5	...	24.	...	4.0
	Inner red		...	...	6.2	...	78.	...	10.
	Outer red		...	0.026	0.21	0.63	5.0	0.15	1.2
GL 490[e]	Outer blue	61	...	0.0084	0.067	0.32	2.5	0.13	1.0
	Inner blue		...	...	2.3	...	19.	...	2.1
	Inner red		...	...	1.9	...	18.	...	2.1
	Outer red		...	0.018	0.14	0.60	4.8	0.21	1.6
NGC 2071[e]	Outer blue	73	>17	0.0049	0.039	0.14	1.1	0.043	0.34
	Inner blue		...	...	0.28	...	3.9	...	0.55
	Inner red		...	...	0.28	...	2.7	...	0.28
	Outer red		...	0.0029	0.023	0.083	0.67	0.027	0.21
W28 A2	Outer blue	40	>94	0.16	1.3	7.0	56.	3.2	26.
	Inner blue		...	...	38.	...	500.	...	75.
	Outer red		...	0.14	1.1	4.6	37.	1.5	12.
GL 2591[e]	Outer blue	55	>16	0.030	0.24	0.66	5.3	0.15	1.2
	Inner blue		...	...	31.	...	240.	...	19.
	Inner red		...	...	2.1	...	23.	...	2.7
	Outer red		...	0.0048	0.038	0.12	0.94	0.029	0.23
S140	Outer blue	58	>23	0.0072	0.057	0.23	1.9	0.080	0.64
	Inner blue		...	...	12.	...	93.	...	7.6
	Inner red		...	...	13.	...	64.	...	3.5
	Outer red		...	0.022	0.18	0.42	3.3	0.085	0.68
Cepheus A[e]	Outer blue	58	...	0.0045	0.0036	0.14	1.2	0.053	0.42
	Inner blue		...	...	1.6	...	13.	...	1.1
	Inner red		...	...	6.9	...	65.	...	6.4
	Outer red		>17	0.027	0.22	0.81	6.5	0.27	2.1

[a] The isotopic abundance ratio, [CO]/[^{13}CO] (Langer & Penzias 1990).
[b] Lower limits of T_{ex} calculated from eqn. (3) assuming $\phi = (3/2)^2$.
[c] Assuming that the sources are neutral atomic wind.
[d] Assuming that the sources are swept-up molecular gas.
[e] Maps cover only the central portions of the outflows.

It is hard to determine ϕ, but we can calculate a very firm lower limit to T_{ex} by assuming a point source centered in both beams [i.e., $\phi = (3/2)^2$]. Although some maps show extended sources, the EHV wind may have a complex structure in position-velocity space that does not allow us to use extended emission to rule out a large value of ϕ.

Table 5 shows the lower limits to T_{ex} calculated from equation (3); they range from 16 to 94 K, indicating that at least some of the EHV gas is warm. If ϕ is closer to unity, the temperatures must be much higher. For example, if $\phi = 3/2$, an intermediate value between that expected for a point source and the value for an extended source, T_{ex} ranges from 30 K to >250 K. Any mixture of cooler gas will produce a lower ratio; for example, applying this method to mixtures of two temperature components, with equal optical depth, would yield an average of the two temperatures. The high observed ratios are thus a strong indication that the bulk of the EHV gas is quite warm.

Equation (3) cannot be used to calculate the excitation temperature in the inner wings because they are not, in general, optically thin. An alternative procedure would be to calculate the excitation temperature from the ratio of the two optical depths deduced from $^{iso}R_3$ and $^{iso}R_2$ (for example, Snell et al. 1984; Margulis & Lada 1985). While this method reduces systematic uncertainties due to beam filling, it can seriously underestimate T_{ex} if components with different optical depths are present (Appendix B). Consequently, we have not estimated T_{ex} in the inner wings, but we show in the next section that knowledge of T_{ex} is not essential for determining column densities.

3.3. *Column Density*

The column density of CO for each channel, N_i^{CO} was calculated from the intensity of the CO $J = 3 \rightarrow 2$ line from

$$N_i^{CO} = 1.10 \times 10^{15} \frac{T_{R3-2}\,\Delta V}{D(n, T_K)} \frac{\tau_{32}}{1 - \exp(-\tau_{32})}, \quad (5)$$

FIG. 3.—(*a*) The same as Fig. 1*a* for NGC 2071. There is a narrow ($\Delta V \approx 20$ km s^{-1}) spectral feature at $\sim$55 km s^{-1} near the southwestern edge of our map, consistent with the feature found by Chernin & Masson (1992). (*b*) The same as Fig. 1*b* for NGC 2071. Maps were made with a 9″ grid. Markers indicate IRS 4, IRS 2, IRS 3, and IRS 1 (*filled circles*) from northeast to southwest (Persson et al. 1981) and an H_2O maser source (*open triangle*) from Genzel & Downes 1979). The bipolar nature of the outflow is clear although our map does not completely cover the blue and red peaks (cf. Bally 1982). Chernin & Masson (1992) have mapped the EHV gas to larger distance and found that it covers a smaller region than the HV gas. (*c*) The same as Fig. 1*c* for NGC 2071. The isotopic ratio, $^{iso}R_2$, in the inner wings agrees well with that of Snell et al. (1984). The interpretation of the line ratios is uncertain for this source because none of the wings have a peak at the central position. Both $^{iso}R_3$ and $^{iso}R_2$ show the typical rise toward the outer wings. The red side of $^{iso}R_3$ and the blue side of $^{iso}R_2$ seem to decrease beyond $|V - V_0| \approx 15$ km s^{-1}, but the uncertainties are very large. The ratio $^{12}R_{32}$ rises only to the red side of the spectrum.

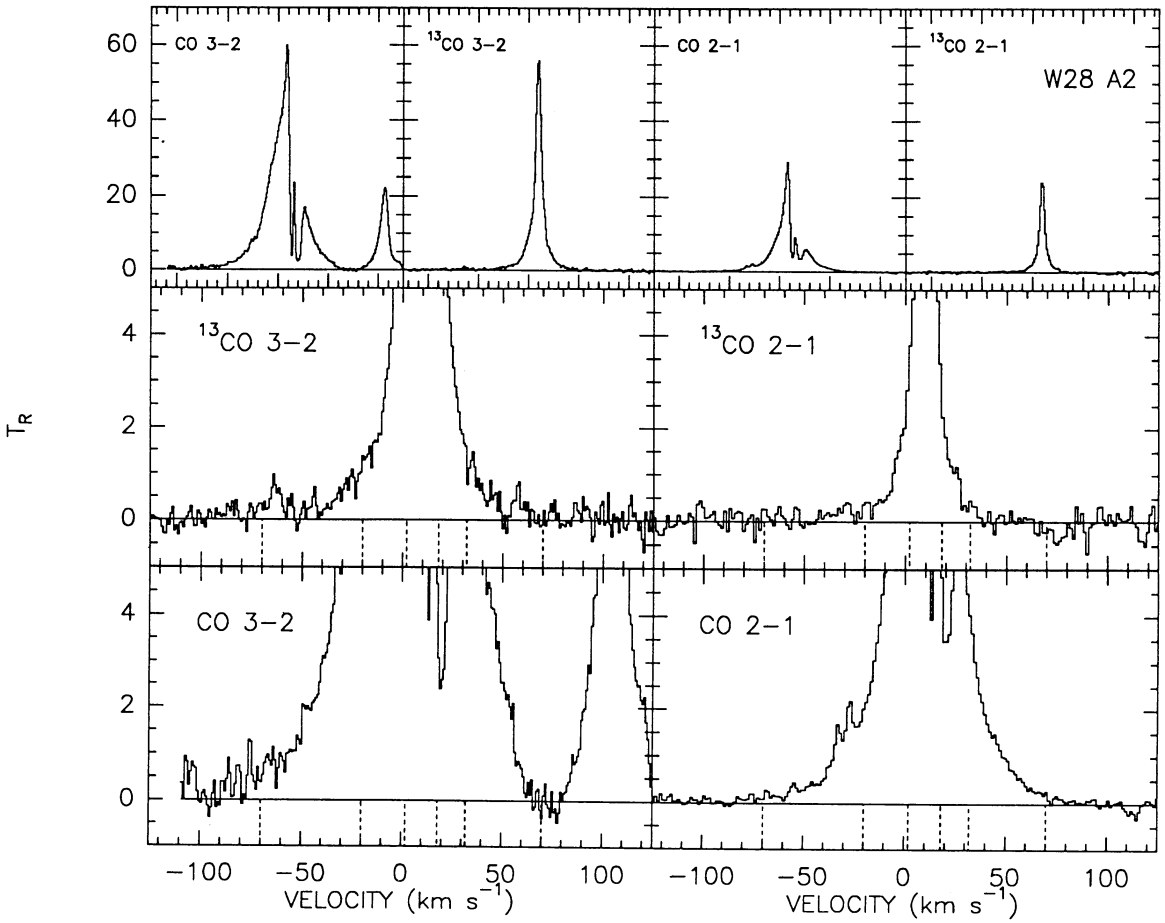

FIG. 4*a*

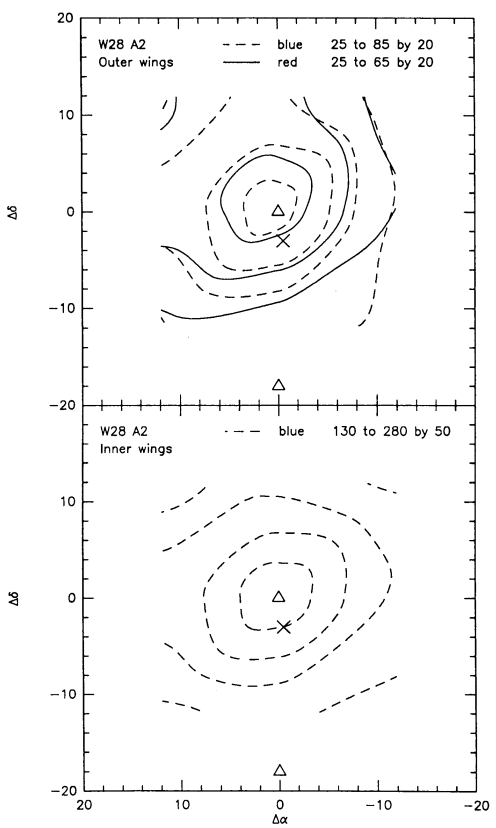

FIG. 4*b*

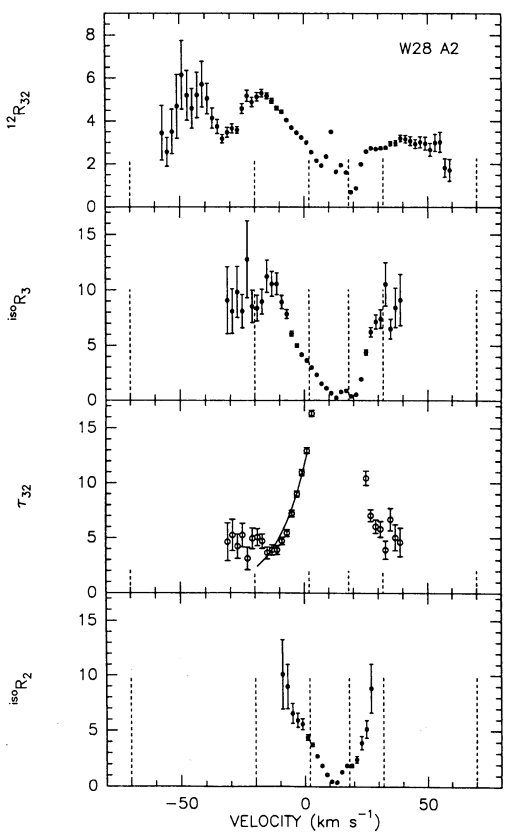

FIG. 4*c*

where

$$D(n, T_K) = f_2[J_\nu(T_{ex}) - J_\nu(T_{bk})][1 - \exp(-16.597/T_{ex})], \quad (6)$$

ΔV is the channel width in km s^{-1}, and f_2 is the fraction of CO molecules in the $J = 2$ state. N_i^{CO} is in units of cm^{-2} and ΔV in km s^{-1}. The optical depth, τ_{32}, was assigned as described in § 3.1. Assuming that the optical depth is known, the main uncertainty is the value of the function $D(n, T_K)$. If all the levels are not in LTE, $D(n, T_K)$ depends on the density, as well as the temperature, through the factor f_2. The LTE assumption can lead to large overestimates of N^{CO} for high temperature and modest density.

Although T_{ex} is not well known, LVG simulations show that $D(n, T_K)$ does not vary much within reasonable intervals of density, n, and kinetic temperature, T_K (Fig. 8). Therefore, we assumed $D(n, T_K) = 1.5$ in our calculations, which is correct to less than a factor of 2 for $10 < T_K < 200$ K and $10^4 < n < 10^6$ cm^{-3}. Column densities derived from $J = 3 \rightarrow 2$ line are somewhat less uncertain than those derived from the $J = 1 \rightarrow 0$ line because $D(n, T_K)$ varies from 0.074 to 0.76 for the $J = 1 \rightarrow 0$ transition in the same intervals of n and T_K.

3.4. *Mass per Channel: Two Possibilities*

The mass per channel, M_i, can be computed from the column density per channel, N_i^{CO}, the distance, d (Table 2), and the solid angle subtended by emission in that channel, Ω, by

$$M_i = \mu m_H d^2 \Omega N_i^{CO} \frac{[H]}{[C]} \frac{[C]}{[CO]}, \quad (7)$$

where $\mu = 1.3$, m_H is the mass of a hydrogen atom, and $[H]/[C] = 2.5 \times 10^3$ (Grevasse et al. 1991). The final factor, $[C]/[CO]$, is about 8 in ambient molecular gas (Dickman 1978; van Dishoeck et al. 1992), with the missing carbon presumably tied up in solid matter. For stellar winds from low-mass young stars, calculations indicate that molecule formation precedes dust grain formation, so that all C is in CO for $\dot{M} > 10^{-4}\ M_\odot$ yr^{-1} (Glassgold et al. 1991). If correct, these models say that a given N_i^{CO} would imply 8 times less matter if the CO emission from a wind than if it arises from swept-up gas. Because the $[C]/[CO]$ ratio in winds from more massive stars is not well known, we will begin by assuming that carbon is fully associated into CO.

In calculating mass, momentum, and energy in the next section, we give two different results for the EHV gas (Table 5), one for a stellar wind, with $[C]/[CO] = 1$, and one for swept-up gas, with $[C]/[CO] = 8$. Since the HV gas is always assumed to be swept up, we give only one result for it.

3.5. *Mass, Momentum, and Kinetic Energy*

The mass, momentum, and kinetic energy of each outflow were calculated from

$$M = \sum_i M_i, \quad (8)$$

$$P = \sum_i M_i |V_i - V_0|, \quad (9)$$

and

$$E_K = \sum_i \tfrac{1}{2} M_i (V_i - V_0)^2, \quad (10)$$

with summations over the velocity channels, i, within each wing interval; V_0 is the central velocity (see Table 4) of the ^{13}CO $J = 2 \rightarrow 1$ line (W3 IRS 5 and Cepheus A) or ^{13}CO $J = 3 \rightarrow 2$ line (all other sources). Since we made no corrections to the velocities for projection effects, the momenta and kinetic energies in Table 5 are lower limits.

Our estimates agree reasonably well with previous work. The total momentum in the wings of W3 IRS 5 is about 80% that found by Mitchell, Hasegawa, & Schella (1992), who included some low velocities in their red wing that we do not count as wing emission. Because the GL 490 maps of Snell et al. (1984) and Mitchell et al. (1992) cover a larger area than ours, their estimates of the mass, momentum, and kinetic energy of the HV outflow from CO $J = 2 \rightarrow 1$ and $J = 1 \rightarrow 0$ observations are about 3–4 times larger than ours. The estimates of the masses, momenta, and kinetic energies of NGC 2071 by Chernin & Masson (1992) are larger (by a factor of about 5 for the outer wings and a factor of about 2 for the inner wings), mostly because their map is larger than ours. The W28 A2 outflow is much more energetic than the others in this paper. Our estimates of the momentum of the outflow agree with Harvey & Forveille (1988), considering the slightly different definitions of the wings and the fact that we do not include the inner red wing. The blue outflows of GL 2591 are much more energetic and massive than the red outflows. Mitchell et al. (1992) also found this asymmetry between the blue and red outflows. The mass of the combined red and blue HV outflows is about twice the mass calculated by Mitchell et al. (1992) when their values are corrected to our distance. Our estimates of the mass, momentum, and kinetic energy of the HV outflows of S140 are consistent with those of Snell et al. (1984), but exceed those of Hayashi et al. (1987), who did not see the full extent of even the HV wings. Our estimate of the mass in the HV flow of Cepheus A is about 2.5 times that of Ho et al. (1982).

3.6. *Driving Force*

In § 4, we will consider the possibility that the EHV wing comes from CO in the actual stellar wind. If the stellar wind drives the HV flow, the average driving force in the wind must equal the average force applied to the HV gas. The force is calculated from

$$F = \frac{P}{t} = \frac{P^2}{MR}, \quad (11)$$

FIG. 4.—(*a*) The same as Fig. 1*a* for W28 A2. The peak at $V = 100$ km s^{-1} in the CO $J = 3 \rightarrow 2$ spectrum is the CS $J = 7 \rightarrow 6$ line in the other sideband. Note that even the CS line is as extended as our inner wings, which suggests that the inner wings are emitted by dense gas (Plume, Jaffe, & Evans 1992). The baseline of the CO $J = 3 \rightarrow 2$ line is quite poor because of the broad CS line. Since the inner red wing of CO $J = 3 \rightarrow 2$ contains a dip which may be either emission in the reference beam or self-absorption, we define the inner red wing using the ^{13}CO $J = 3 \rightarrow 2$ line. (*b*) The same as Fig. 1*b* for W28 A2. Maps were made with a 12″ grid. The map of the inner red wing is omitted because the spectra contain a dip. Markers indicate H_2O maser sources (*open triangles*) from Genzel & Downes (1977), and a compact H II region (*crosses*) from Wood & Churchwell (1989). The contour map shows a compact source with both blue and red wings peaking at the position of an infrared source and H_2O maser and also well within the extent of the radio continuum emission. (*c*) The same as Fig. 1*c* for W28 A2. The line ratios in the outer wings are somewhat unreliable because of poor baselines. The ratios $^{iso}R_2$ and $^{iso}R_3$ rise toward the wings until they become undefined, which indicates that the optical depth is getting smaller as the velocity increases.

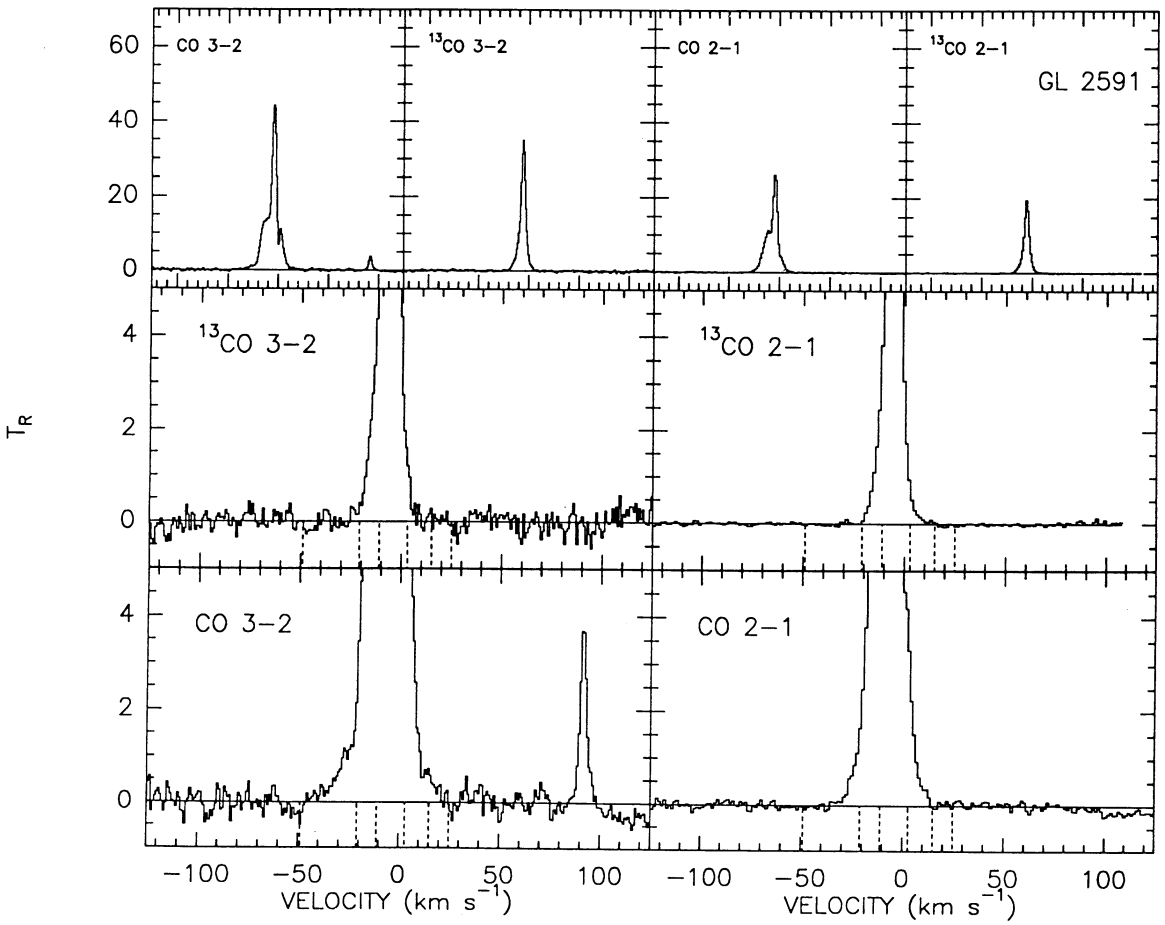

FIG. 5*a*

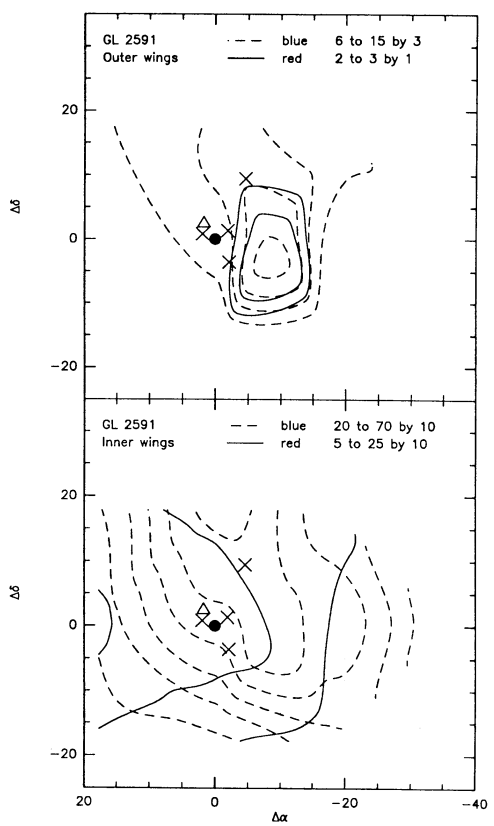

FIG. 5*b*

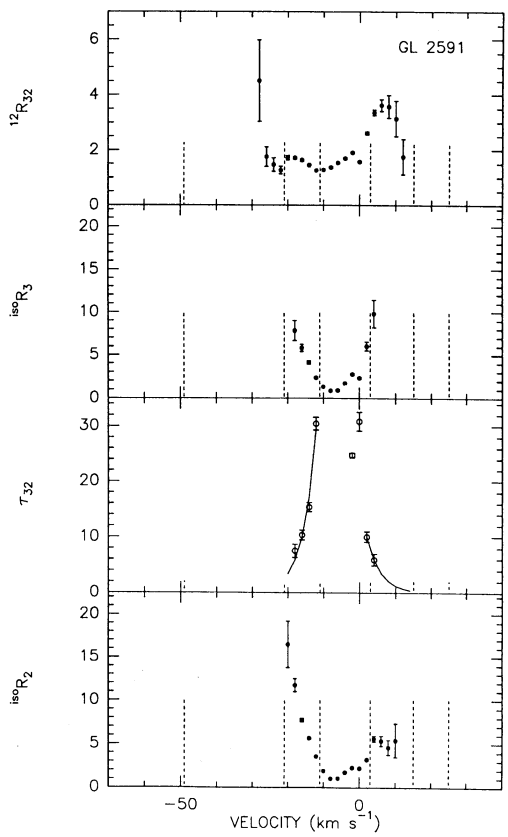

FIG. 5*c*

where $t = R/V_{ch}$ is the characteristic timescale for the outflow, R is the size of the outflow, and $V_{ch} = P/M$ is the characteristic (mass-weighted) velocity.

The ratio of driving force in the EHV wing to the average force required to sweep up the HV wing was calculated from

$$R_F = \frac{F_{EHV}}{F_{HV}} = \frac{R_P^2}{R_R R_M}, \quad (12)$$

where R_P, R_R, and R_M are ratios of momentum, size, and mass, respectively. It is hard to determine R_R from the maps for most of our sources. Since our maps and maps from previous work (see references in Table 6) show that the spatial extents of the EHV and the HV outflows are similar (within a factor of ~ 2), we assumed $R_R = 1$ in our calculations. This is not true for GL 2591, which shows a very compact EHV source along with extended HV outflows. So the correct R_F of GL 2591 should be larger than the value listed in Table 6. Because the correction factor for projection should be similar for the HV and EHV outflows, ratios of quantities for the EHV and HV outflows should be unaffected by projection effects.

Table 6 shows R_F for all of our sources and for some EHV outflows observed by others. Unlike our classification, the wings of HH 7–11 (Koo 1990) and IRAS 0328 + 3035 (Bachiller et al. 1991) are divided into HV, IHV (intermediate high velocity), and EHV wings. For these two sources, we show two values in Table 6, $(F_{EHV} + F_{IHV})/F_{HV}$ and $F_{EHV}/(F_{IHV} + F_{HV})$. Also NGC 7538 IRS 9 (Mitchell & Hasegawa 1991) has an EHV wing detected only to the red side of the spectrum. Again, we list two values in Table 6, F_{RedEHV}/F_{RedHV} and $F_{RedEHV}/(F_{RedHV} + F_{BlueHV})$.

Table 6 also shows the characteristic timescale for the EHV outflows $t = R/V_{ch}$. When the map shows a clear separation between blue and red lobes, the size of the outflow, R, is calculated from the distance between red and blue peaks. If the blue lobe is superposed on the red lobe, we take the size of the FWHM contour as R. Projection effects, not corrected for in our calculation, can increase (if flow is in the plane of the sky) or decrease (if flow is along the line of sight) the timescale by substantial factors. In addition, t would be smaller if used the maximum velocity, as is often done, rather than V_{ch}. On the other hand, Parker, Padman, & Scott (1991) have argued on the basis of detection statistics that timescales derived from this method must underestimate the true ages of outflows, by an order of magnitude on average.

3.7. *Other Information*

Since the discussion in § 4 will need the luminosity and production rate of ionizing photons, these are given in Table 6. The luminosity was taken from the literature, corrected if necessary to the distances we have adopted. The rate of production of Lyman-continuum photons, N_L, was calculated from

$$N_L = 7.5 \times 10^{43} \nu^{0.1} d^2 S_\nu T_e^{-0.45}, \quad (13)$$

where N_L is in units of s^{-1}, ν the frequency in GHz, d the distance in kpc, S_ν the radio continuum flux in mJy, and T_e the electron temperature in units of 10^4 K (Rubin 1968). We assumed $T_e = 8000$ K and used the radio data given in Table 6. To avoid optical depth problems, we used the highest frequency radio continuum data available which was not judged to be contaminated by dust emission.

In some of these sources, the radio continuum emission may arise in an ionized stellar wind. In these cases, N_L calculated using equation (13) will overestimate the production of Lyman-continuum photons because Balmer-continuum photons may also ionize the dense winds (Thompson 1984). We have computed the mass loss rates in ionized winds ($\dot{M}_{ionized}$) by assuming that all the radio emission in Table 6 comes from an ionized wind. We have used equation (30) of Panagia (1991), appropriate for a spherical, isothermal wind, and assumed a terminal wind velocity of 300 km s^{-1} and an electron temperature of 10^4 K. If the wind is confined to a narrow jet, this equation will overestimate the mass-loss rate (Reynolds 1986). In addition, any contribution to S_ν from an optically thin H II region will cause us to overestimate $\dot{M}_{ionized}$.

For comparison, we have also calculated the mass-loss rate in the stellar wind based on the HV CO emission, assuming momentum conservation, using

$$\dot{M}_{CO} = \frac{P}{t v_w}, \quad (14)$$

where P and t are the momentum and timescale for the HV flow, and v_w is the stellar wind velocity, assumed to be 300 km s^{-1}. $\dot{M}_{ionized}$ and $\dot{M}_{CO}$ are given in Table 6. In cases where our maps are incomplete, $\dot{M}_{CO}$ will be underestimated, but if Parker et al. (1991) are right about the ages of outflows, $\dot{M}_{CO}$ based on the usual method will be overestimated. In defense of the traditional method, we note that Natta & Giovannardi (1990) derived mass loss rates from Na I lines for several stars which agreed very well with rates derived from CO.

4. CONCLUSIONS

In this section, we will summarize the results and then consider different ideas for the origin of the EHV gas and the nature of the stellar wind.

4.1. *Summary of Results*

Our detection of EHV wings was a result of serendipity while conducting a CS study. The selection criteria involved detections of dense gas rather than any knowledge of molecu-

FIG. 5.—The same as Fig. 1*a* for GL 2591. The peak at $V = 90$ km s^{-1} is the CS $J = 7 \rightarrow 6$ line. (*b*) The same as Fig. 1*b* for GL 2591. Maps were made with an 18″ grid. Markers indicate an infrared source (*filled circles*) from Lada et al. (1985), an H_2O maser source (*open triangles*) from Wynn-Williams et al. (1977), and radio continuum peaks (*crosses*) from Campbell (1984). The integrated intensities of the inner wings do not peak within our map. The CO $J = 2 \rightarrow 1$ map of Mitchell et al. (1991) shows that the peaks of the inner wings are indeed beyond the boundaries of our map. Both outer wings clearly have compact emission peaked at the same position. In this region, the H_2O maser source, the infrared source, and the strongest radio continuum source are all displaced from each other, lying along a NE-SW line. The peak of the outer wing emission is displaced from all these sources, but is closest to the radio continuum source. The offset from all the sources is smaller than the beam size, but larger than the combined pointing uncertainties and positional uncertainties of the maser and infrared source. If observations with higher resolution confirm this offset, it would suggest that the source of radio continuum emission, rather than the infrared source, drives the outflow. (*c*) The same as Fig. 1*c* for GL 2591. The ratios $^{iso}R_3$ and $^{12}R_{32}$ have minima at the line center and rise toward the line wings until they become undefined, suggesting that the outer wings are optically thin. Since only one channel in the inner red wing has a well-defined $^{iso}R_3$, we included the outermost channel of the line core to make the τ_{32} fit.

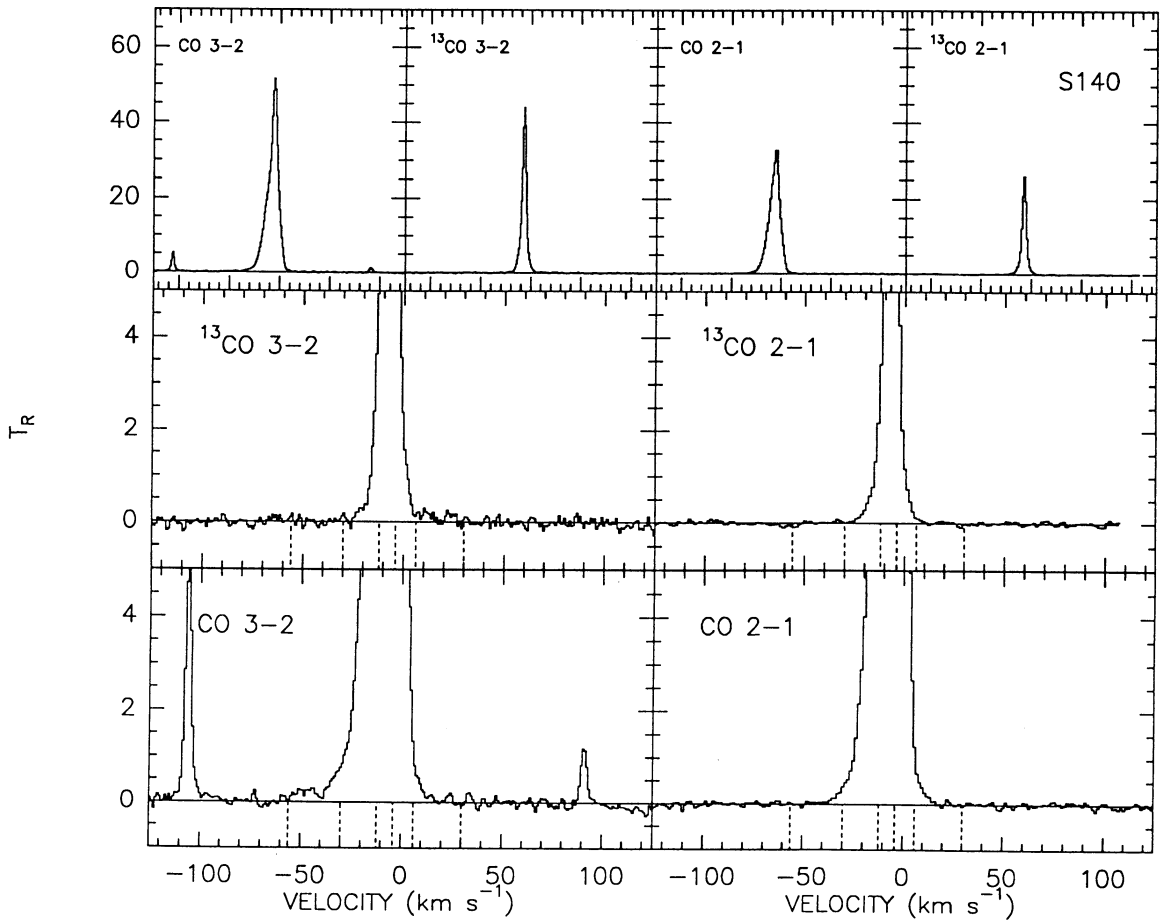

FIG. 6*a*

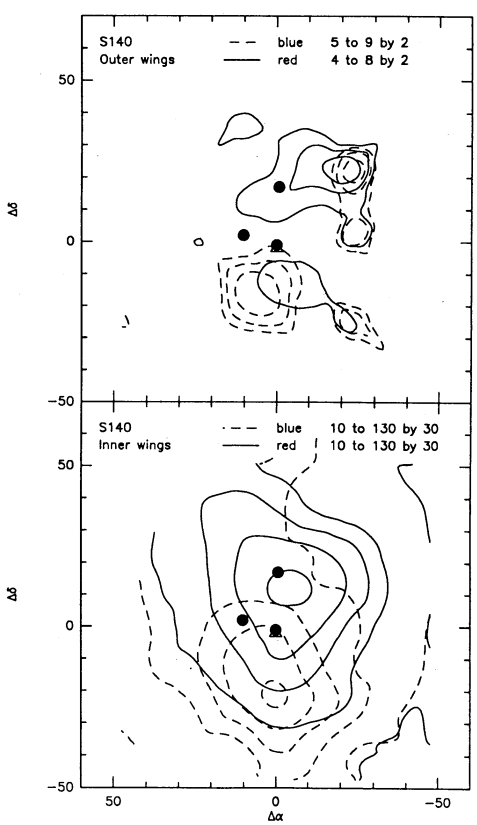

FIG. 6*b*

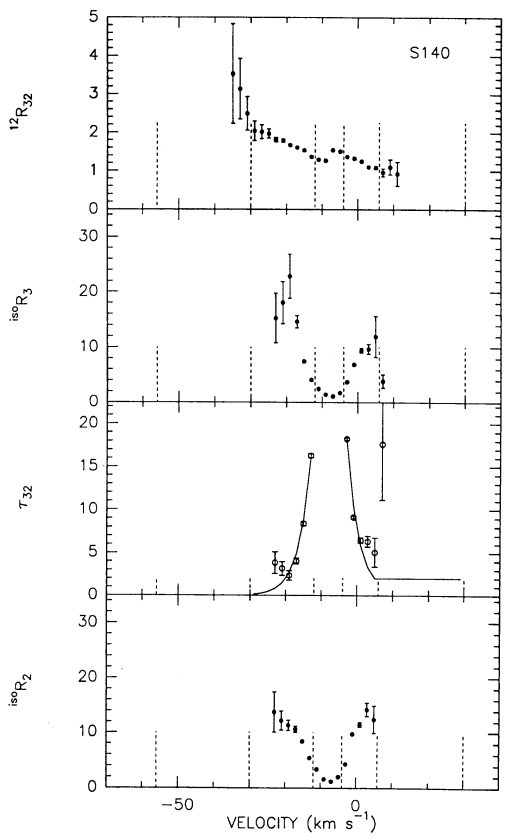

FIG. 6*c*

lar outflows, although all the sources were known to have HV outflows. Thus, it is probably significant that almost all the sources in the study did show EHV wings. EHV outflows are apparently common in regions similar to those in our sample, dense regions of moderate to high mass star formation, with luminosities ranging from 500 $L_\odot$ to 4×10^5 $L_\odot$.

The $J = 3 \rightarrow 2$ line of CO shows the EHV wings more clearly than lower J lines, indicating that it is a good way to search for EHV gas, given an appropriate receiver and site. The high ratio of the $J = 3 \rightarrow 2$ to $J = 2 \rightarrow 1$ EHV wing emission indicate that the EHV gas is generally (GL 490 is an exception) optically thin and warm ($T_{ex} > 20$–90 K). While the formal limits on T_{ex} in Table 5 are not very high, these limits assume the highest possible value for the ratio of filling factors. Lower values of this ratio would produce much higher T_{ex}, comparable to the temperatures needed to excite the CO $J = 14 \rightarrow 13$ and $J = 16 \rightarrow 15$ lines observed toward many of these sources (Stacey 1992), and impossibly high in some cases. Howe et al. (1987) have detected $J = 14 \rightarrow 13$ line of CO toward NGC 2071. They remark that the warm component responsible for the far-infrared CO emission can account for the high-velocity gas seen in the millimeter CO lines if the density is near 5×10^4 cm^{-3} and the temperature of the gas lies between 250 and 750 K.

The spectra indicate molecular gas moving at characteristic velocities (in the sense of momentum over mass) of at least 20–40 km s^{-1} with respect to the cloud rest velocity, without projection corrections. It is hard to accelerate molecular gas to such high velocities without dissociation. Based on the size of the outflows, these velocities result in characteristic times of 1600–4200 yr. Thus, these stars have been producing stellar winds, probably neutral winds, within quite recent times, even though many now are producing enough ionizing photons to have substantial H II regions. One explanation, particularly attractive in distant, very obscured regions, is that the source driving the outflow is separate from the source producing the ionizing photons. In the case of S140, however, the evidence points to IRS 1 as the source of the neutral wind, even though it may be a main sequence star (Evans et al. 1989).

In contrast to recent spectroscopy of nearby, less luminous sources with EHV gas, our spectra are dominated by fairly smooth profiles, with discrete velocity features being rare; in addition the maps show clumpy emission only in the case of S140. On the other hand, our maps are often incomplete or not completely sampled. The weakness of the EHV wings, together with their likely high T_{ex}, suggests a low filling factor, which could result from many small clumps. In this case, the smooth profiles could just be a result of inadequate spatial resolution. Another shared spectral characteristic is the presence of distinct changes of slope between the EHV and HV wings, with the slope discontinuities in NGC 2071 and GL 2591 being the most dramatic.

4.2. *Nature of the EHV Gas*

We consider a quantitative test of the hypothesis that the EHV gas traces the stellar wind. Giovanardi et al. (1992) have shown that the H I winds in L1551 and HH 7–11 are sufficient to drive the HV molecular outflow by momentum conservation. We apply a similar test to the EHV gas, traced in our case by CO. In Table 6, we give R_F, the ratio of the force available in the EHV gas to that required to produce the momentum in the HV gas, averaged over the lifetime of the HV flow. We also include R_F for some previously studied sources.

While the ratios for previously studied sources are consistent with unity within likely uncertainties, the ratios for our sources are not. The largest ratio found in our observations is 0.10 (GL 490) and the average is 0.045. Low ratios appear to rule out the stellar wind interpretation for our sources, but there are several reasons to suspend judgement. Since the EHV gas is spread over a large range of velocities, sensitivity limitations could cause an underestimate of the emission. Second, our division between HV and EHV gas is not precise in sources without clear spectral breaks; moving the boundary between HV and EHV gas to lower velocities would raise the ratios. Examples of this effect can be seen in the different ratios for HH 7–11 and IRAS 03282+3035, depending on whether the intermediate-velocity wing is assigned to the HV or EHV wings. Third, by drawing our boundaries in velocity rather than fitting a series of Gaussians, we are neglecting gas at low *projected* velocities, a more serious omission for the EHV gas than for the HV gas. Fourth, incomplete maps in some sources introduce uncertainties; for example, the data of Chernin & Masson (1992) yield R_F about 3 times our value for NGC 2071. These four factors typically introduce factor of 2–3 uncertainties, so are unlikely to change the conclusions.

Perhaps more important is our assumption that all the C is associated into CO in calculating R_F for the stellar wind hypothesis. If, on average, only 4.5% of the C is in CO, the average R_F would be unity. The chemical calculations of Glassgold et al. (1991) find CO abundances as low as [CO]/[C] = 0.04 only for low mass-loss rates ($\dot{M} \lesssim 3 \times 10^{-6}$ $M_\odot$ yr^{-1}), but our EHV outflow sources have much larger mass-loss rates ($\dot{M} > 10^{-4}$ $M_\odot$ yr^{-1}). However, the calculations of Glassgold et al. (1991) were for cool ($T_* = 5000$ K) stars, while the stars in this study are much more luminous and most are producing some ionizing photons. Ionizing and dissociating photons from these stars may cause lower CO abundances in the wind. Glassgold et al. (1991) did consider a model with $\dot{M} = 3 \times 10^{-6}$ $M_\odot$ yr^{-1} which had a $T_* = 6000$ K. Even this modest increase in T_* caused the CO abundance to drop by three orders of magnitude. Glassgold et al. (1991) also note that they have ignored dust formation in the wind which could shield molecules.

We need models of winds from stars with $L > 500$ $L_\odot$ and

FIG. 6.—The same as Fig. 1*a* for S140. The CO $J = 3 \rightarrow 2$ spectrum shows two CS $J = 7 \rightarrow 6$ lines (at $V = -105$ and 90 km s^{-1}) because it is a sum of data taken during two periods when the source had two different topocentric velocities. (*b*) The same as Fig. 1*b* for S140. Maps were made with a 12″ grid. Markers indicate infrared and radio sources, IRS 2, IRS 1, and IRS 3 (*filled circles*) clockwise from the top (Hackwell, Grasdalen, & Gehrz 1982; Evans et al. 1989), and an H_2O maser source (*open triangles*) from Genzel & Downes (1979). The inner wings show a clear bipolar pattern (cf. Hayashi et al. 1987). The contour map of the outer wings looks clumpy because of several secondary peaks. S140 is the only source in our sample in which the outer wings appear clumpy. (*c*) The same as Fig. 1*c* for S140. The isotopic ratio, $^{iso}R_2$, of the inner wings is consistent with Snell et al. (1984). Both isotopic ratios rise toward the outer wings. The ratio $^{12}R_{32}$ rises toward the blue wing, but decreases toward the red wing, perhaps a result of observing with different beam sizes a wing whose spatial distribution does not peak at the center of the source; i.e., the CO $J = 2 \rightarrow 1$ beam is larger than the CO $J = 3 \rightarrow 2$ beam and contains more of the red peak. We assumed $\tau_{32} = 2$ in the red wing.

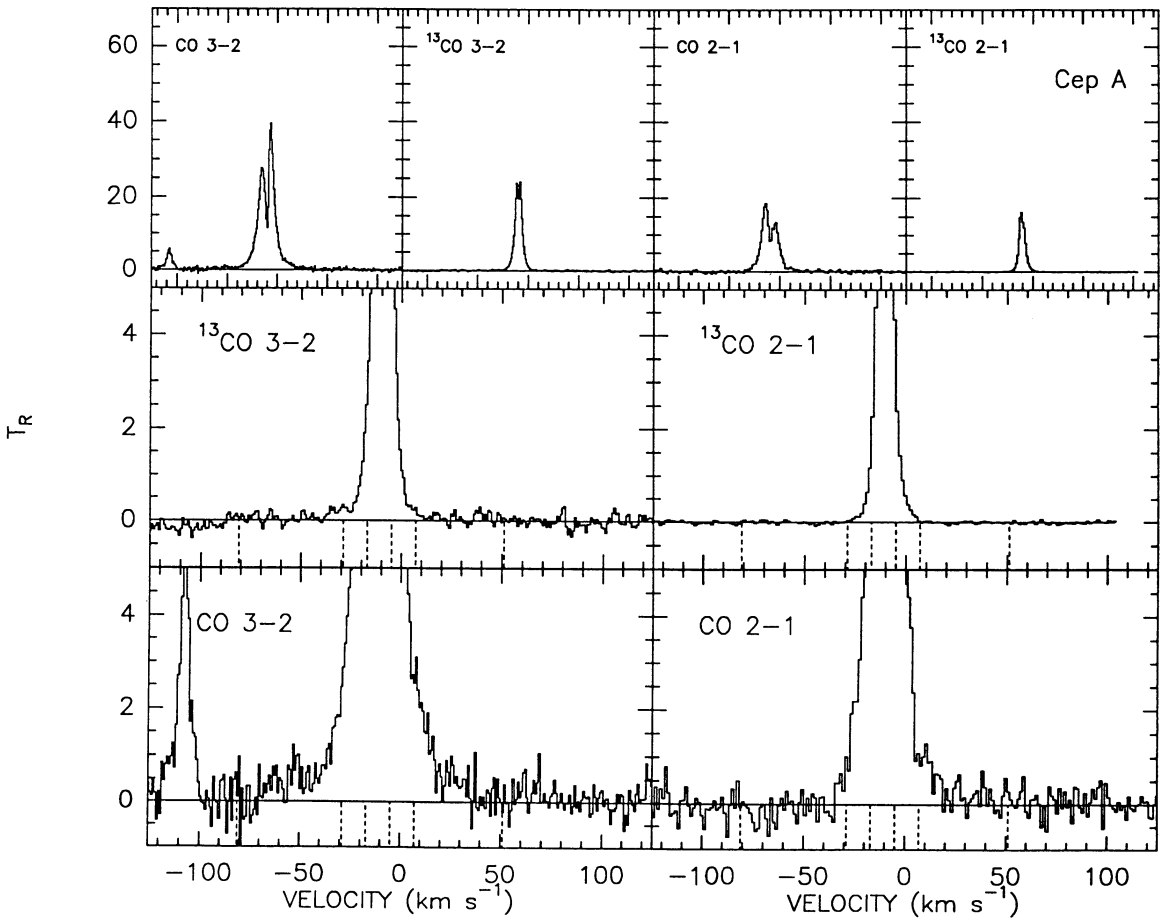

FIG. 7*a*

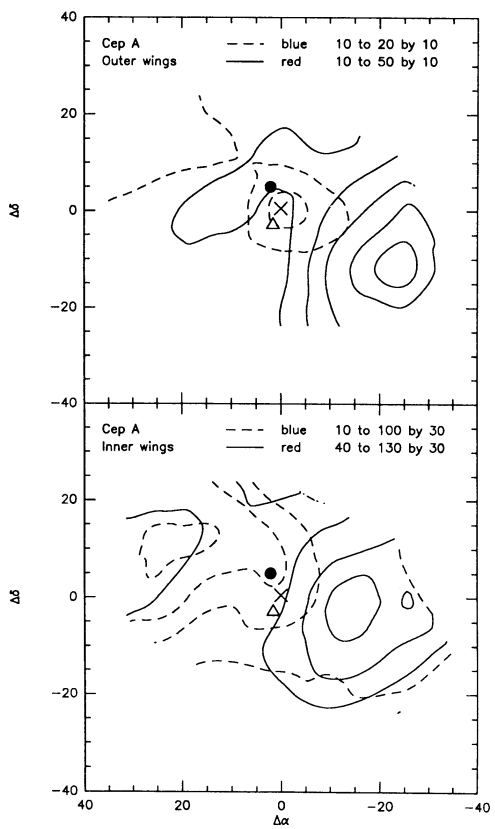

FIG. 7*b*

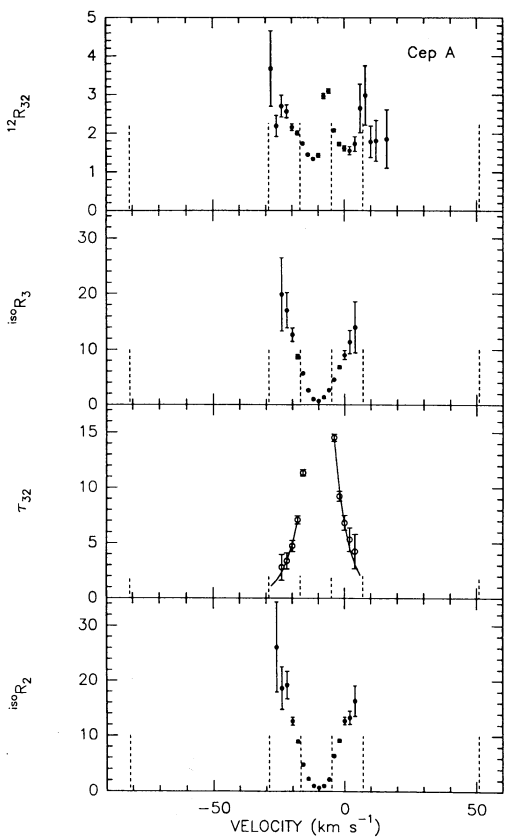

FIG. 7*c*

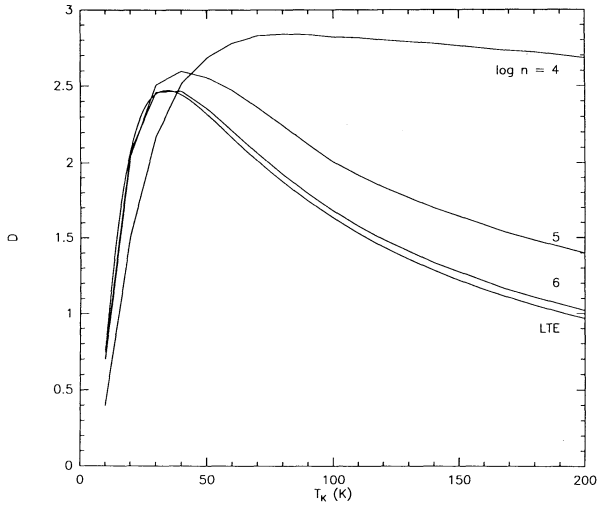

FIG. 8.—$D(n, T_K)$ (defined by eq. [6]) is plotted for reasonable values of n (10^4–10^6 cm^{-3}) and T_K (10–200 K), as calculated from the LVG model, and from the LTE assumption. In the LVG calculations, we assumed a constant CO column density per unit velocity interval, $N/dV = 10^{16}$ cm^{-2} km^{-1} s, typical of our derived values, but $D(n, T_K)$ is insensitive to N/dV.

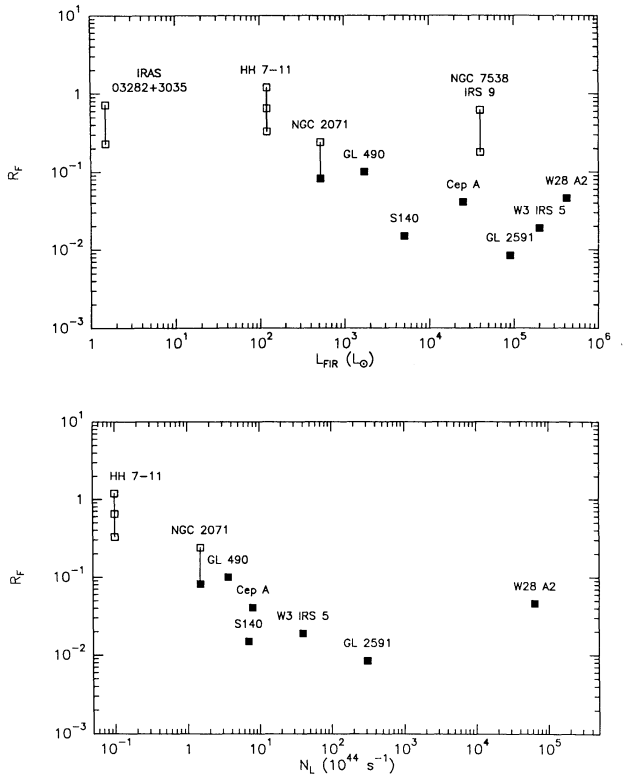

FIG. 9.—The ratio of EHV to HV driving force vs. luminosity (*upper panel*) and the rate of production of Lyman-continuum photons (*lower panel*). We assumed that the EHV gas is the stellar wind ([C]/[CO] = 8). Filled pointers are from this paper, and open pointers are from references given in Table 6. If there are multiple references for one source, corresponding pointers are connected by vertical lines. See Table 6 for details.

higher temperatures to determine CO abundances in the winds. Empirically, we can assess whether the nature of the stars may be affecting the CO abundance by plotting R_F versus luminosity and versus N_L, the rate of production of ionizing photons (Fig. 9). The plots indicate that R_F declines sharply with increasing luminosity and increasing N_L, with the latter trend being particularly striking. If the CO abundance decreases with ionizing photon rate, the EHV CO emission could still be tracing the stellar wind. W28 A2 is unusual in having an impressive EHV wing while producing a large N_L. As a distant and complex region, W28 A2 may be a case in which the outflow is driven by a separate source. However, the outflow must still avoid ionization by the source of the ionizing photons for the extended H II region.

We conclude that an origin for the EHV wings in molecules formed in a neutral wind cannot be clearly ruled out. Even if the EHV CO does arise in the wind, it is not a useful probe of the momentum in high luminosity sources, since the CO is unlikely to be fully associated.

An alternative origin for the EHV gas is ambient gas which has been entrained or swept-up by the wind. In cases where there is a break in the slope in the profile, the process must be distinct from that which produces the HV wing. Chernin & Masson (1992) argue that it is difficult to accelerate molecules to the extremely high velocities without dissociation, so they favor a picture in which the EHV molecules have reformed after the passage of a fast shock. Models of such shocks indicate that the molecules reform when the column density of the shocked material reaches about 1–3 × 10^{20} cm^{-2} (Neufeld & Dalgarno 1989a; Hollenbach & McKee 1989). By $N = 3 \times 10^{20}$ cm^{-2}, the carbon is fully associated, with an abundance of 4×10^{-4}, implying a CO column density of about 1×10^{17} cm^{-2}, and the gas has a temperature of about 500 K. The high temperature is consistent with observations of high-J CO emission in several of our sources (Howe et al. 1987; Stacey et al. 1987) and with our high $^{12}R_{32}$, but our column density estimates for the EHV CO at the central positions range from 2×10^{15} cm^{-2} to 1.2×10^{17} cm^{-2}, with only W28 A2 having the column density expected in this picture. Larger column densities may be present if the emission comes from many small regions, as seems likely on other grounds. The recent detection of SO in NGC 2071 clearly indicates that shock chemistry is active, but the spatial and velocity structure of the SO emission is hard to interpret simply in terms of shock models (Chernin & Masson 1993).

In the picture of outflows proposed by Stahler (1993), the stellar wind sweeps up and entrains gas in a turbulent mixing process, which may allow acceleration to EHV velocities without dissociation. In this case, the original molecular cloud abundances may be preserved, with only 12% of the C in CO. We can then compare the mass, momenta, and energy of the

FIG. 7.—(*a*) The same as Fig. 1*a* for Cepheus A. The peak at $V = -110$ km s^{-1} is CS $J = 7 \rightarrow 6$ line. (*b*) The same as Fig. 1*b* for Cepheus A. Maps were made with a 12″ grid. Markers indicate a mid-infrared source (*filled circles*) from Beichman, Becklin, & Wynn-Williams (1979), radio component 2 of Hughes (1985) (*crosses*), and an H_2O maser source (*open triangles*) from Lada et al. (1981). The contour maps clearly show the bipolar nature of the inner wings. The outer wings, however, show a rather complex structure. The outer blue wing has a local peak at the center position, while the red wing has a displaced peak. The peak of the blue wing coincides within the uncertainties with an H_2O maser source and a radio continuum source. (*c*) The same as Fig. 1*c* for Cepheus A. The ratios $^{iso}R_3$ and $^{iso}R_2$ have minima at the line center and rise toward the line wings until the denominators become less than the thresholds. Since $^{12}R_{32}$ is also consistent with low τ_{32}, we have assumed optically thin emission in the outer wings.

TABLE 6

RATIOS OF DRIVING FORCES AND RELATED QUANTITIES

SOURCE	EHV CO				HV CO	FAR-INFRARED		RADIO CONTINUUM				
	R_F[a]	R_F[b]	References	t[c] (yr)	$\dot{M}_{CO}$ (10^{-5} $M_\odot$ yr^{-1})	L_{FIR} ($L_\odot$)	References	ν (GHz)	S^ν (mJy)	References	log N_L[d] (s^{-1})	$\dot{M}_{ionized}$ (10^{-5} $M_\odot$ yr^{-1})
A. Our Observations												
W3 IRS 5	0.019	0.15	1	3100	4.8	200,000	2	15.4	7.0	3	45.6	1.1
GL 490	0.10	0.82	1	2300	1.3	1700	4	23.1	3.2	5	44.6	0.14
NGC 2071	0.082	0.66	1	3200	0.3	520	6	15.0	9.2[e]	7	44.2	0.09
W28 A2	0.046[f]	0.36[f]	1	1900	56.4	420,000	8	15.0	6540.5	9	48.8	280.
GL 2591	0.0085	0.068	1	2000	6.8	90,000	10	5.0	79.4[g]	11	46.5	9.1
S140	0.015	0.12	1	4200	5.2	5000[h]	12	15.0	7.7[h]	13	44.8	0.29
Cepheus A	0.041	0.32	1	1600	2.8	25,000	14	23.1	13.2[i]	5	44.9	0.26
Average	0.045	0.36		2600								
B. Previous Observations												
HH 7–11	1.2[j]	9.8[j]	15	...	...	115[l]	16	5.0	0.8[m]	7	43.0	0.02
HH 7–11	0.65[k]	5.2[k]	15									
HH 7–11	0.33	2.7	17									
IRAS 03282+3035	0.72[j]	5.7[j]	18	...	...	$\leq$1.5	18	...	...	...	...	...
IRAS 03282+3035	0.23[k]	1.8[k]	18									
NGC 2071	0.24	1.9	19									
NGC 7358 IRS 9	0.62[n]	4.9[n]	20	...	...	40,000	20	...	...	...	...	...
NGC 7538 IRS 9	0.18[o]	1.5[o]	20									

[a] Ratio of driving forces assuming the EHV outflow is the stellar wind ([C]/[CO] = 1).
[b] Ratio of driving forces assuming the EHV outflow is swept-up molecular gas ([C]/[CO] = 8).
[c] Characteristic timescale of the EHV outflow.
[d] Rates of production of Lyman-continuum photons.
[e] From NGC 2071 IRS 1 alone.
[f] From blue outflows only.
[g] From GL 2591 (1) alone.
[h] From S140 IRS 1 alone.
[i] From Cepheus A (2) alone.
[j] Assumes IHV outflow is part of EHV outflow.
[k] Assumes IHV outflow is part of HV outflow.
[l] From SVS 13 alone.
[m] From NGC 1333 (5) alone.
[n] From red EHV and red HV outflows only.
[o] From blue HV, red EHV, and red HV.

REFERENCES.—(1) This paper; (2) Werner et al. 1990; (3) Colley 1980; (4) Harvey et al. 1979 (corrected according to our distance); (5) Simon et al. 1983; (6) Butner et al. 1990; (7) Snell & Bally 1986; (8) Emerson, Jennings, & Moorwood 1973; (9) Wood & Churchwell 1989; (10) Lada et al. 1984; (11) Campbell 1984; (12) Lester et al. 1986; (13) Evans et al. 1989; (14) Koppenaal et al. 1979 and Evans et al. 1981; (15) Koo 1990; (16) Cohen & Schwartz 1987; (17) Bachiller & Cernicharo 1990; (18) Bachiller et al. 1991; (19) Chernin & Masson 1992; (20) Mitchell & Hasegawa 1991.

EHV gas to that of the HV gas, using the second columns for each in Table 5. It is clear that the HV gas carries most of the mass and momentum in all cases; in a few cases, the energy in the EHV wings is comparable to that in the HV wings, but it is usually not. Thus, the EHV wings, if swept-up matter, do not change the overall energetics of the outflows. The R_F values are still less than 1 (Table 6), but the ratios are now sufficiently close (0.36 in the average) that uncertainties could explain the difference. In the picture of Stahler, in which momentum is transferred through turbulent mixing, one might expect a similar force to have been applied to gas at all velocities.

A different model of outflows, with collimated jets as the driving source, has been suggested recently (Masson & Chernin 1993; Raga et al. 1993). Jets are plausible driving sources only if Parker et al. (1991) are correct in arguing that traditional analyses have underestimated lifetimes and overestimated $\dot{M}_{CO}$ by a factor of 10. In the jet models, the EHV CO emission is produced by the bow shock, where the jet encounters the ambient cloud. This simple model would predict a single EHV feature at the end of each lobe, rather than an extended wing, but Masson & Chernin (1993) proposed that the jets wander, producing multiple EHV blobs. Whether this model can reproduce the rather smooth EHV wings and the large velocity extents that we observe remains to be seen.

In general, the picture of the EHV wings as gas originally in the ambient cloud is certainly plausible. However, this picture provides no obvious explanation for the rather striking trend of R_F with N_L in Figure 9, nor for the fact that $R_F \sim 1$ in some sources with low luminosity and N_L.

4.3. *Where is the Carbon in the Wind?*

If the EHV material is, in fact, ambient material swept up by a faster stellar wind, we would still need to find the underlying stellar wind driving both the HV and EHV components. In young low-luminosity stars, ionized winds, if they are present at all, are insufficient to sweep up the molecular gas (Evans et al. 1987). The situation for more luminous objects is less clear. In Table 6, we compare mass-loss rates inferred from the radio emission ($\dot{M}_{ionized}$) with the stellar wind $\dot{M}$ inferred from the HV CO ($\dot{M}_{CO}$) assuming momentum conservation (eq. [14]). Only GL 490 and radio component 2 in Cepheus A actually have the properties expected for spherical winds, and $\dot{M}_{ionized}$ for those sources is an order of magnitude less than $\dot{M}_{CO}$. The estimates of $\dot{M}_{ionized}$ are upper limits for the other sources, and $\dot{M}_{CO}$ estimates are often lower limits. Still, only W28 A2 and GL 2591 have $\dot{M}_{ionized}$ comparable to $\dot{M}_{CO}$. The radio source in GL 2591 does not coincide with the infrared source, making its status unclear. W28 A2 has been classified as an ultracompact H II region with a shell structure (Wood & Churchwell 1989) and its radio emission is too strong to arise in an ionized wind.

The best interpretation of the radio continuum results for our sources is that the true value of $\dot{M}_{ionized}$ is much less than $\dot{M}_{CO}$ in all of the sources in the sample. This leads to the conclusion that the winds are primarily neutral, even in these more luminous objects. Detection of H I wings toward DR 21 (Russell et al. 1992) supports the idea that luminous stars may also have neutral winds. How a star producing a substantial number of ionizing photons also drives a neutral stellar wind is a puzzle worthy of theoretical consideration. We will confine ourselves to asking where is the carbon in the stellar wind? Since these are oxygen-rich objects, the carbon is unlikely to be found in solid particles, leaving CO, C^0, and C^+ as possibilities.

In low luminosity sources, the carbon may well be in CO and already detected since $R_F \sim 1$. Observations of H I in some low-luminosity sources over large velocity intervals indicates that there is atomic or molecular material at velocities up to 150 km s^{-1} from line center (Lizano et al. 1988; Giovanardi et al. 1992). Could we have detected wings of this width if the gas contains enough CO to make $R_F = 1$? A wind with a rectangular profile and a terminal velocity of 150 km s^{-1} would produce a brightness temperature less than 0.2 K in the $J = 3 \rightarrow 2$ line of CO for all sources except W28 A2, where it would be more like 2 K. Given that ± 150 km s^{-1} would extend to the ends of our baseline and given the systematic uncertainties in the baselines, it would be difficult for us to rule out the existence of this kind of CO component, even if the spectral shape had some degree of central peaking. Continuing improvements in instrumentation and observing techniques may eventually permit a meaningful search for even higher velocity molecular gas.

Another possibility is that the C is neutral and atomic. We have estimated the strength of the EHV wings in $^3P_1 \rightarrow {}^3P_0$ for the sources in our sample, assuming that the gas is hotter than 50 K, all of the carbon not in CO is in C^0, and the force in the EHV wind matches that in the molecular HV wind. With these assumptions, it should be possible to detect C^0 emission from the EHV gas in at least half the sources in our sample. For most, the [C I] line would be detectable at some EHV velocities even if $[C^0]/[C]$ is as low as 0.1. Walker et al. (1993) have observed HV wings in the $^3P_1 \rightarrow {}^3P_0$ transition of C I at 492 GHz in several sources, including three of the sources discussed in this paper. They found that the C^0 abundance was comparable to the abundance in quiescent cloud material. Walker et al. (1993) would not have been able to detect EHV wings, but longer integration time under good conditions should be able to determine if a substantial fraction of the carbon in the stellar wind is C^0.

The carbon could also be in the form of C^+, if it is ionized by stellar photons. High-velocity shocks could also produce substantial ultraviolet emission, but shock models for dense gas predict C^+ column densities which are always less than those of CO (Neufeld & Dalgarno 1989b). The strong trend for R_F to decrease as N_L increases may indicate a chemical shift from CO to C^+, due to the stellar ultraviolet emission. Estimates based on assumptions similar to those used for [C I] predict strong [C II] emission from a mostly C^+ wind. The sensitivity of current airborne spectrometers to the 158 μm $^2P_{3/2} \rightarrow {}^2P_{1/2}$ line is sufficient, in principle, to place meaningful limits on the amount of C^+ in the EHV winds in our sources, but practical limitations would make it very hard to detect very weak, broad wings on a narrow bright line in the far-infrared.

While the observations are difficult, failure to detect C in any form at the level required by the usual analysis of the CO HV flows would support the idea that outflow ages have been underestimated and lend credence to models of jet-driven outflows.

We thank John E. Howe, Jeffrey G. Mangum, René Plume, Constance E. Walker, Yangsheng Wang, Lianzhou Yu, and Shudong Zhou for acquiring some of the data. We wish to thank L. M. Chernin for helpful comments. This work was supported by NSF grant AST 90-17710, by a grant from the W. M. Keck Foundation, by a grant from the Texas Advanced Research Program to the University of Texas, and by a David and Lucile Packard Foundation Fellowship.

APPENDIX A

THE BEHAVIOR OF $^{12}R_{32}$

To understand the general behavior of $^{12}R_{32}$, we can simplify equation (2) by assuming that the optical depths follow the LTE relation (eq. [4]). The largest possible value of the ratio of beam filling factors, ϕ is $(3/2)^2$, assuming a point source centered in both beams. The resulting $^{12}R_{32}$ is plotted in Figure 10 as a function of the optical depth for various values of excitation temperature. For an optically thick cloud, $^{12}R_{32}$ is quite insensitive to both τ and T_{ex}. For an optically thin cloud, $^{12}R_{32}$ can be as low as 0.44 (for $T_{ex} = 10$ K and $\phi = 1$) and as high as $(3/2)^4$ [for $T_{ex} \rightarrow \infty$ and $\phi = (3/2)^2$] depending on the temperature and source extent. Therefore, $^{12}R_{32}$ larger than $\sim(3/2)^2$ implies that the cloud is optically thin, but $^{12}R_{32}$ smaller than $\sim(3/2)^2$ does not give any clue to the physical conditions unless the source extent is known.

One might regard $^{12}R_{32}$ as a good temperature indicator for optically thin clouds based on Figure 10, but it is hard to determine ϕ, the ratio of beam filling factors. The lower limits to T_{ex} in Table 5 were obtained by assuming a point source. In addition, mixtures of gas at different temperatures will result in an estimate of T_{ex} less than that of the hotter gas. If both components have equal optical depth, the derived temperature is close to the average of the two components, according to simulations that we have done. Simulations with two equal temperature components of differing optical depth, but both still optically thin, show that the true temperature will be somewhat underestimated by this method. Thus, the excitation temperatures we have derived from this method should be regarded as quite strong lower limits.

APPENDIX B

TEMPERATURE ESTIMATES FROM THE CO OPTICAL DEPTH RATIO

It is in principle possible to determine the excitation temperature from the ratio of the optical depths of two adjacent transitions assuming LTE and, in the process, avoid some of the problems with beam filling factors alluded to in Appendix A. Consider two transitions, CO $J + 1 \rightarrow J$ (labeled by u) and CO $J \rightarrow J - 1$ (labeled by l); then

$$\frac{\tau_u}{\tau_l} = \frac{J+1}{J} \frac{1 - \exp(-h\nu_u/kT_{ex})}{\exp(h\nu_l/kT_{ex}) - 1} . \quad \text{(B1)}$$

Snell et al. (1984) and Margulis & Lada (1985), using this method for several outflows with CO $J = 2 \rightarrow 1$ and CO $J = 1 \rightarrow 0$ data (calculating τ_{21} and τ_{10} from $^{iso}R_2$ and $^{iso}R_1$ using eq. [1]), found oddly low excitation temperatures ($T_{ex} = 6.5$–25 K) except in Ori A. Although we have determined optical depths of CO $J = 3 \rightarrow 2$ and CO $J = 2 \rightarrow 1$ lines for most of the inner wings and some of the outer wings, we did not use this method to calculate the excitation temperatures. The reason is that outflows may be clumpy and there may be several unresolved components in our main beam.

Assuming that there are two components, A and B, in our main beam, one with τ_{uA} and the other with τ_{uB}, but both with the same excitation temperature, T_{ex}, then τ_{lA} and τ_{lB} can be deduced by equation (B1). The observed radiation temperature is roughly the sum of those from each component. The procedure would derive the optical depths $\tau_{u,obs}$ and $\tau_{l,obs}$, assuming all the filling factors

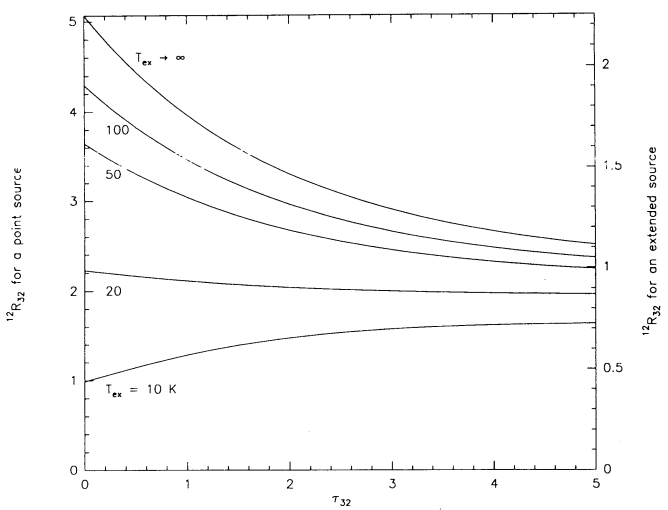

FIG. 10.—$^{12}R_{32}$ as a function of τ_{32} for various T_{ex}. It is assumed that τ_{21} follows eq. (4). Numbers on the left vertical axis are for $\phi = (3/2)^2$ (point source), and those on the right vertical axis are for $\phi = 1.0$ (extended source).

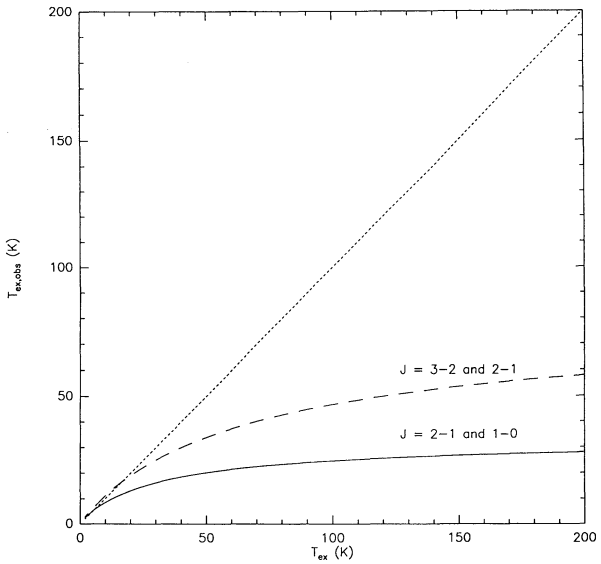

FIG. 11.—The observed excitation temperature, $T_{ex,obs}$, as a function of the real excitation temperature, T_{ex}, with two components in the beam. It is assumed that $X = 56$, $\tau_{uA} = 1$, $\tau_{uB} = 10$, $T_{exA} = T_{exB}$, and all the filling factors are the same. The solid curve is for the combination of CO $J = 2 \rightarrow 1$ and CO $J = 1 \rightarrow 0$, and the dashed curve is for the combination of CO $J = 3 \rightarrow 2$ and CO $J = 2 \rightarrow 1$ transitions. The straight dotted line is $T_{ex,obs} = T_{ex}$.

are about the same, from

$$\frac{1 - \exp(-\tau_{obs})}{1 - \exp(-\tau_{obs}/X)} = \frac{1 - \exp(-\tau_A) + 1 - \exp(-\tau_B)}{1 - \exp(-\tau_A/X) + 1 - \exp(-\tau_B/X)}, \quad \text{(B2)}$$

where τ can be either τ_u or τ_l.

The resulting $T_{ex,obs}$ (excitation temperature calculated by eq. [B1]) is shown as a function of T_{ex} (real excitation temperature of the cloud) in Figure 11, assuming two components with equal filling factor with one component having $\tau = 1$ and the other $\tau = 10$. These curves clearly show that this method can fail badly as a temperature estimator if there are two or more components of different optical depth in the beam. The qualitative result is true for any pair of opacities as long as they differ by a factor of 2–3 or more and the component with larger opacity has $\tau > 1$. If the low temperatures derived by this method from the $J = 2 \rightarrow 1$ and $J = 1 \rightarrow 0$ data are an artifact of using the technique in the presence of inhomogeneities in the sources, Figure 11 shows that a similar analysis using the $J = 3 \rightarrow 2$ and $J = 2 \rightarrow 1$ transition should yield higher temperatures. Indeed, the typical T_{ex}'s we derive by this method are twice those derived in the earlier work with the $J = 2 \rightarrow 1$ and $J = 1 \rightarrow 0$ lines.

REFERENCES

Anthony-Twarog, B. J. 1982, AJ, 871, 1213
Bachiller, R., & Cernicharo, J. 1990, A&A, 239, 276
Bachiller, R., Cernicharo, J., Martín-Pintado, J., Tafalla, M., & Lazareff, B. 1990, A&A, 231, 174
Bachiller, R., & Gómez-González, J. 1992, Astron. Astrophys. Rev., 3, 257
Bachiller, R., Martín-Pintado, J., & Planesas, P. 1991, A&A, 251, 639
Bally, J. 1982, ApJ, 261, 558
Bally, J., & Lada, C. J. 1983, ApJ, 265, 824
Beichman, C. A., Becklin, E. E., & Wynn-Williams, C. G. 1979, ApJ, 232, L47
Blaauw, A., Hiltner, W. A., & Johnson, H. L. 1959, ApJ, 130, 69
Butner, H. M., Evans, N. J., II, Mundy, L. G., Natta, A., & Randich, M. S. 1990, ApJ, 364, 164
Campbell, B. 1984, ApJ, 287, 334
Chernin, L. M., & Masson, C. R. 1992, ApJ, 396, L35
———. 1993, ApJ, 403, L21
Claussen, M. J., et al. 1984, ApJ, 285, L79
Cohen, M., & Schwartz, R. D. 1987, ApJ, 316, 311
Colley, D. 1980, MNRAS, 193, 495
Crampton, D., & Fisher, W. A. 1974, Pub. Dom. Ap. Obs., 14, 12
Dickman, R. L. 1978, ApJS, 37, 407
Emerson, J. P., Jennings, R. E., & Moorwood, A. F. M. 1973, ApJ, 184, 401
Evans, N. J., II. et al. 1981, ApJ, 244, 115
Evans, N. J., II, Levreault, R. M., Beckwith, S., & Skrutskie, M. 1987, ApJ, 320. 364
Evans, N. J., II, Mundy, L. G., Kutner, M. L., & DePoy, D. L. 1989, ApJ, 346, 212
Forster, J. R., Welch, W. J., & Wright, M. C. H. 1977, ApJ, 215, L121
Fukui, Y., Iwata, T., Mizuno, A., Bally, J., & Lane, A. P. 1993, in Protostars and Planets III, ed. E. H. Levy & J. Lunine (Tucson: Univ. of Arizona Press), in press
Genzel, R., & Downes, D. 1977, A&AS, 30, 145
Genzel, R., & Downes, D. 1979, A&A, 72, 234
Georgelin, Y. M., & Georgelin, Y. P. 1976, A&A, 49, 57
Giovanardi, C., Lizano, S., Natta, A., Evans, N. J., II, & Heiles, C. 1992, ApJ, 397, 214
Glassgold, A. E., Mamon, G. A., & Huggins, P. J. 1989, ApJ, 336, L29
———. 1991, ApJ, 373, 254
Grevasse, N., Lambert, D. L., Sauval, A. J., van Dishoeck, E. F., Farmer, C. B., & Norton, R. H. 1991, A&A, 242, 488
Hackwell, J. A., Grasdalen, G. L., & Gehrz, R. D. 1982, ApJ, 252, 250
Harvey, P. M., Campbell, M. F., Hoffman, W. F., Thronson, H. A., Jr., & Gatley, I. 1979, ApJ, 229, 990
Harvey, P. M., & Forveille, T. 1988, A&A, 197, L19
Hayashi, M., Hasegawa, T., Omodaka, T., Hayashi, S. S., & Miyawaki, R. 1987, ApJ, 312, 327
Ho, P. T. P., Moran, J. M., & Rodríguez, L. F. 1982, ApJ, 262, 619
Hollenbach, D., & McKee, C. F. 1989, ApJ, 342, 306
Howe, J. E., Jaffe, D. T., Genzel, R., Stacey, G. J., Townes, C. H., & Lugten, J. B. 1987, BAAS, 19, 1015
Hughes, V. A. 1985, ApJ, 298, 830
Koo, B.-C. 1989, ApJ, 337, 318
———. 1990, ApJ, 361, 145
Koppenaal, K., Sargent, A. I., Nordh, L., van Duinen, R. J., & Aalders, J. W. G. 1979, A&A, 75, L1
Kraus, J. D. 1966, Radio Astronomy (New York: McGraw Hill)
Kutner, M. L., & Ulich, B. L. 1981, ApJ, 250, 341
Lada, C. J. 1985, ARA&A, 23, 267
Lada, C. J., Blitz, L., Reid, M. J., & Moran, J. M. 1981, ApJ, 243, 769
Lada, C. J., Thronson, H. A., Smith, H. A., Schwartz, P. R., & Glaccum, W. 1984, ApJ, 286, 302
Langer, W. D., & Penzias, A. A. 1990, ApJ, 357, 477
Lester, D. F., Harvey, P. M., Joy, M., & Ellis, H. B., Jr. 1986, ApJ, 309, 80

Lizano, S., Heiles, C., Rodríguez, L. F., Koo, B.-C., Shu, F. H., Hasegawa, T., Hayashi, S., & Mirabel, I. F. 1988, ApJ, 328, 763
Mangum, J. G. 1993, PASP, in press
Margulis, M., & Lada, C. J. 1985, ApJ, 299, 925
Margulis, M., & Snell, R. L. 1989, ApJ, 343, 779
Masson, C. R., & Chernin, L. M. 1993, ApJ, in press
Masson, C. R., Mundy, L. G., & Keene, J. 1990, ApJ, 357, L25
McGregor, P. J., Persson, S. E., & Cohen, J. G. 1984, ApJ, 286, 609
Merrill, K. M., & Soifer, B. T. 1974, ApJ, 189, L27
Mitchell, G. F., & Hasegawa, T. I. 1991, ApJ, 371, L33
Mitchell, G. F., Hasegawa, T. I., & Schella, J. 1992, ApJ, 386, 604
Mitchell, G. F., Maillard, J.-P., & Hasegawa, T. I. 1991, ApJ, 371, 342
Natta, A., & Giovanardi, C. 1990, ApJ, 356, 646
Natta, A., Giovanardi, C., Palla, F., & Evans, N. J., II 1988, ApJ, 327, 817
Neufeld, D. A., & Dalgarno, A. 1989a, ApJ, 340, 869
———. 1989b, ApJ, 344, 251
Panagia, N. 1991, in The Physics of Star Formation and Early Stellar Evolution, ed. C. J. Lada & N. D. Kylafis (Dordrecht: Kluwer), 565
Parker, N. D., Padman, R., & Scott, P. F. 1991, MNRAS, 252, 442
Persson, S. E., Geballe, T. R., Simon, T., Lonsdale, C. J., & Baas, F. 1981, ApJ, 251, L85
Phillips, J. P., et al. 1988, A&A, 190, 289
Plambeck, R. L., Snell, R. L., & Loren, R. B. 1983, ApJ, 266, 321
Plume, R., Jaffe, D. T., & Evans, N. J., II 1992, ApJS, 78, 505
Raga, A. C., Cantó, J., Calvet, N., Rodríguez, L. F., & Torrelles, J. M. 1993, A&A, in press
Reynolds, S. P. 1986, ApJ, 304, 713
Richardson, K. J., White, G. J., Avery, L. W., Lesurf, J. C. G., & Harten, R. H. 1985, ApJ, 290, 637
Richer, J. S., Hills, R. E., & Padman, R. 1992, MNRAS, 254, 525
Rodríguez, L. F., & Cantó, J. 1983, Rev. Mexicana Astr. Ap., 8, 163
Rubin, R. H. 1968, ApJ, 154, 391
Ruden, S. P., Glassgold, A. E., & Shu, F. H. 1990, ApJ, 361, 546
Russell, A. P. G., Bally, J., Padman, R., & Hills, R. E. 1992, ApJ, 387, 219
Simon, M., Felli, M., Cassar, L., Fischer, J., & Massi, M. 1983, ApJ, 266, 623
Snell, R. L., & Bally, J. 1986, ApJ, 303, 683
Snell, R. L., Loren, R. B., & Plambeck, R. L. 1980, ApJ, 239, L17
Snell, R. L., Scoville, N. Z., Sanders, D. B., & Erickson, N. R. 1984, ApJ, 284, 176
Stacey, G. J. 1992, private communication
Stacey, G. J., Jaffe, D. T., Lugten, J. B., Genzel, R., & Townes, C. H. 1987, BAAS, 19, 1016
Stahler, S. W. 1993, in Astrophysical Jets, ed. M. Livio, C. O.Dea, & D. Burgarella (Cambridge: Cambridge Univ. Press), in press
Thompson, R. I. 1984, ApJ, 283, 165
van Dishoeck, E. F., Glassgold, A. E., Guelin, M., Jaffe, D. T., Neufeld, D., Tielens, A. G. G. M., & Walmsley, C. M. 1992, in IAU Symp. 150, Astrochemistry of Cosmic Phenomena, ed. P. D. Singh (Dordrecht: Kluwer), 285
Walker, C. K., Narayanan, G., Büttgenbach, T. H., Carlstrom, J. E., Keene, J., & Phillips, T. G. 1993, in preparation
Werner, M. W., et al. 1980, ApJ, 242, 601
Wood, D. O. S., & Churchwell, E. 1989, ApJS, 69, 831
Wynn-Williams, C. G., Becklin, E. E., Forster, J. R., Matthews, K., Neugebauer, G., Welch, W. J., & Wright, M. C. H. 1977, ApJ, 211, L89
Wynn-Williams, C. G., Becklin, E. E., & Neugebauer, G. 1972, MNRAS, 160, 1